This is a preprint, the final version is subject to change, of the American Mineralogist (MSA)
Cite as Authors (Year) Title. American Mineralogist, in press.
DOI: https://doi.org/10.2138/am-2019-6983

Investigation of the kieserite–szomolnokite solid solution series, $(Mg,Fe)SO_4 \cdot H_2O$, with relevance to Mars: a study on crystal chemistry, FTIR- (5200–400 cm^{-1}) and Raman- (4000–100 cm^{-1}) spectroscopy under ambient and Martian temperature conditions

Revision 1

Dominik Talla[a*], Manfred Wildner[a]

[a] Institut für Mineralogie und Kristallographie, Althanstraße 14, 1090 Wien, Austria
*corresponding author (dominik.talla@univie.ac.at)

Abstract

The investigation of hydrous sulfate deposits and sulfate-cemented soils on the surface of Mars is one of the important topics in the recent scientific endeavor to retrieve detailed knowledge about the planetary water budget and surface weathering processes on our neighbor planet. Orbital visible/near-IR spectra of the Martian surface indicate kieserite, $MgSO_4 \cdot H_2O$, as a dominant sulfate species at lower latitudes. However, given the Fe-rich composition of the Martian surface, it is very probable that its actual composition lies at an intermediate value along the solid solution series between the kieserite and szomolnokite ($FeSO_4 \cdot H_2O$) endmembers. Despite the known existence of significant lattice parameter changes and spectral band position shifts between the two pure endmembers, no detailed crystal chemical and spectroscopic investigation along the entire kieserite–szomolnokite solid solution range has been done yet.

The present work proves for the first time the existence of a continuous kieserite–szomolnokite solid solution series and provides detailed insight into the changes in lattice parameters, structural details, and positions of prominent bands in FTIR- (5200–400 cm^{-1}) and Raman- (4000–100 cm^{-1}) spectra in synthetic samples as the Fe/Mg ratio progresses, at both ambient as well as Mars-relevant lower temperatures. Additionally, an UV-Vis-NIR (29000–3500 cm^{-1}) crystal field spectrum of szomolnokite is presented to elucidate the influence of Fe^{2+}-related bands on the overtone- and combination mode region.

The kieserite–szomolnokite solid solution series established in this work shows Vegard-type behavior, i.e., lattice parameters as well as spectral band positions change along linear trends. The presented detailed knowledge of these trends enables useful semi-quanitative estimations of the Fe/Mg ratio that can be applied to interpret Martian monohydrated sulfates in data from remote sensing missions on a global scale as well as from in-situ rover measurements. Given the knowledge of the surface temperature during spectral measurements, the established temperature behavior allows quantitative conclusions concerning the Fe/Mg ratio. Our understanding of the kieserite–szomolnokite solid solution series will be well applicable to the Mars 2020 and ExoMars 2020 rover missions that will focus on near IR (0.9 to 3.5 μm) and, for the first time on Mars, Raman spectroscopy.

Keywords: Kieserite–szomolnokite solid solution, Mars mineralogy, crystal chemistry, FTIR spectroscopy, Raman spectroscopy, UV-Vis-NIR spectroscopy

This is a preprint, the final version is subject to change, of the American Mineralogist (MSA)
Cite as Authors (Year) Title. American Mineralogist, in press.
DOI: https://doi.org/10.2138/am-2019-6983

Introduction

The surprising discovery of large amounts of sulfate minerals on the Martian surface dates from the late 1970s, when Viking landers carried out the first in-situ analyses of Martian soils. Using X-ray fluorescence spectroscopy, the presence of diverse Mg- and Ca-dominated sulfate salts was anticipated, in addition to NaCl (Keil et al. 1978; Clark and Van Hart 1981). The sulfates are presumed to originate from acidic weathering of basaltic rock-forming minerals such as olivine and pyroxene, which are believed to contain significant amounts of Fe (Christensen et al. 2004; Schröder et al. 2004; Morrison et al. 2018). Further in-situ measurements of the soil composition confirming sulfates took place at Meridiani Planum and Gusev crater using data from the APXS (Alpha Particle X-ray Spectrometer), Mössbauer instrument, and the Mini-TES (Miniature Thermal Emission Spectrometer) on the Opportunity and Spirit rovers (landed in 2004). The terrain at Meridiani Planum consists of bright, layered sediments cemented by various sulfates – interpreted to be predominantly kieserite, $MgSO_4 \cdot H_2O$, and jarosite, perhaps also minor bassanite, thenardite and some halite (Clark et al. 2005).They extend across vast regions of Meridiani Planum (Christensen et al. 2004; Clark et al. 2005; Glotch et al. 2006) as well as adjacent areas of Terra Meridiani (Arvidson et al. 2005). The formation of the sulfates and the cementation of the sediment by them is believed to have been caused by percolating underground water or sulfate-rich brines with partial contribution from overland flow or body of water (Christensen et al. 2004). However, Knauth et al. (2005) suggest that the observed sedimentary structures could also be ascribed to impact surges from a large nickel-iron meteorite. Papike et al. (2007) note that especially kieserite, via partial Fe-, Ni-, or Co-incorporation, could be an indicator for meteorite impacts as relevant processes in the formation and redistribution of sulfates on Mars.

On a global Martian scale, WEH (Water-Equivalent Hydrogen) maps and OMEGA (Observatoire pour la Minéralogie, l'Eau, les Glaces et l'Activité) data indicate variable, low (in comparison with higher latitudes), but still significant amounts of water bound in minerals and buried water ice in the equatorial regions ranging up to 10 wt% (Feldman et al. 2004; Milliken et al. 2007), despite instability of the latter under the prevailing surface conditions. In general, the data suggest that sulfates of varying hydration state, including kieserite, probably represent the dominant water reservoir and also play a key role in the sulfur cycle at lower (<45°) and equatorial Martian latitudes. (Feldman et al. 2004; Milliken et al. 2007; Gendrin et al. 2005; Bishop et al. 2009; Karunatillake et al. 2014; Noel et al. 2015; Mangold et al. 2008; Roach et al. 2010; Lichtenberg et al. 2010). OMEGA spectra confirmed surficial accumulations of hydrous sulfates (including kieserite) in various regions within Valles Marineris and elsewhere, spatially correlated with layered terrains (Gendrin et al. 2005). High-resolution CRISM (Compact Reconnaissance Imaging Spectrometer for Mars) data offer a more detailed insight into the stratigraphy of such layered sulfate deposits in Juventae Chasma (Bishop et al. 2009; Noel et al. 2015) and West Candor Chasma. In the latter case, Mangold et al. (2008), considering MOLA data (Mars Orbiter Laser Altimeter), found potential indications for kieserite being the primary sulfate cementing the layered terrains, since it is dominant on steeper slopes, while higher sulfate hydrates prevail on the flatter regions where the eroded primary material accumulates and partially rehydrates. Large sulfate deposits with kieserite are known to occur in Ius Chasma (Roach et al. 2010) and Aram Chaos (Lichtenberg et al. 2010), which possibly formed by evaporation of a surface body of water.

Given these finds, as well as the long-term knowledge of the Martian soil containing many Fe-rich phases investigated in greater detail by Dyar and Schaefer (2004) and Dyar et al. (2013), it is very probable that the actual composition of Martian monohydrated sulfates will represent

various intermediate species along the binary join between kieserite and the isotypic Fe endmember szomolnokite, $FeSO_4 \cdot H_2O$, given their partial or complete miscibility. Despite reference data having been obtained from the kieserite and szomolnokite endmembers, showing significant shifts of the spectral features and lattice parameters (Chio et al. 2007; Lane 2007; Lane et al. 2015), no detailed investigation of the crystal chemical and spectral characteristics along the entire kieserite–szomolnokite solid solution series was done so far. However, the structural and crystal chemical evolution along the continuous kieserite–cobaltkieserite solid solution series, $(Mg,Co)SO_4 \cdot H_2O$, was recently investigated by Bechtold and Wildner (2016), indicating that complete miscibility might also be expected for the $(Mg,Fe)SO_4 \cdot H_2O$ system.

In this paper, we present the results of detailed structural, crystal chemical, FTIR and Raman spectroscopic investigations on synthetically prepared members along the kieserite–szomolnokite binary solid solution, $Mg_{1-x}Fe_xSO_4 \cdot H_2O$, at ambient and lower temperatures, as relevant for Mars surface conditions, complemented by UV-Vis-NIR crystal field spectra of Fe^{2+} in szomolnokite. The presented data may prove invaluable in further refining the chemical composition of Martian monohydrated sulfates based on available remote sensing data in the mid-infrared range, as well as be a fundamental dataset for interpreting future in-situ data from forthcoming Mars rovers, in particular data from the SuperCam (Wiens et al. 2017a, 2017b) and SHERLOC (Scanning Habitable Environments with Raman & Luminescence for Organics & Chemicals; Beegle et al. 2014) instruments onboard the Mars 2020 rover (NASA) and the RLS (Raman Laser Spectrometer; Rull et al. 2017; Rull 2018) and ISEM (Infrared Spectrometer for ExoMars; Dobrolenskiy et al. 2017) instruments onboard the ExoMars 2020 rover (ESA).

Experimental

Sample preparation

The hydrothermal technique was used to synthesize crystalline material with a pre-adjusted Mg/Fe ratio along the kieserite–szomolnokite solid solution using Teflon-lined stainless steel autoclaves with an inner volume of ~55 cm^3. Each autoclave was filled with $MgSO_4 \cdot 7H_2O$ and $FeSO_4 \cdot 7H_2O$ amounting to 6 g in total, to obtain a specific Mg/Fe ratio in the resulting crystals; H_2SO_4 (w = 0.73) was added as solvent. All reagents were of analytical grade. Initial problems regarding partial oxidation of Fe^{2+} to Fe^{3+}, leading to the formation of unwanted phases as well (e.g., rhomboclase and other Fe^{3+} or mixed Fe^{2+}/Fe^{3+} sulfates) required the use of a redox buffer.

In a first series of buffered synthesis runs, a foil of metallic iron (dimensions 3 × 10 × 1 mm) was used, with the addition of 25 cm^3 H_2SO_4 (w = 0.73). Despite the positive effect of the foil leading to $(Mg,Fe)SO_4 \cdot H_2O$ forming as practically the sole product, a part of the metal dissolved in the acid, causing the crystals to be significantly enriched in Fe relative to the pre-set Mg/Fe ratio. Hence, these synthesis attempts were stopped after the Mg-dominant batch runs in favor of the preferred use of 5 ml H_2SO_3 (w = 0.06) as the redox buffer instead, added along with 20 cm^3 H_2SO_4 (w = 0.73) as solvent, in all subsequent experiments for the full range of Mg/Fe ratios.

The filled hydrothermal autoclaves were placed into a programmable furnace and heated at a rate of 50 °C/h to 210 °C. Following a holding time of 24 hours to ensure complete dissolution of the contents, a cooling rate of 3 °C/h down to room temperature was applied. After decantation of the acid and mechanical removal of the solids from the reaction vessel, the product was washed twice with distilled H_2O, taking advantage of the relatively slow dissolution rate of the sulfate monohydrates. Following a twofold washing process using 98% ethanol to remove H_2O from the previous step, the product was dried in an oven at 65 °C overnight. The resulting colorless to light beige material was stored in airtight vials. Microscopic inspection showed the

145 batches to consist predominantly of fine crystals (10–50 μm) and crystal aggregates, with
146 sporadic larger individuals (up to ~300μm), the latter revealing dipyramidal habit and
147 pronounced sectoral or polysynthetic twinning.

148 To our surprise, the crystals, as long as they are free of residues of the parent solution, are
149 stable in air over long time scales (years to decades; even original crystals of $FeSO_4 \cdot H_2O$ from
150 the syntheses of Wildner and Giester 1991 are still preserved), with only close-to-endmember
151 $MgSO_4 \cdot H_2O$ slowly transforming to higher hydrates.

152

153 **Chemical analyses and powder X-ray diffraction**

154 Wet-chemical analyses were done on a part of each sample batch at the Masaryk University
155 in Brno, Czech Republic. An amount of ~0.5 g of ground sample material was dissolved in
156 boiling HNO_3 (w = 0.65). Contents of Mg and Fe were both determined by atomic absorption
157 analysis (instrument Solaar M5 - TJAsolutions, measurement time 4 s per element) with an
158 analytical error of 0.005 wt% for Mg and 0.002 wt% for Fe.

159 A further part of each sample batch was examined using powder X-ray diffraction. The
160 material was pressed onto an Si-holder and measured on a Philips PW 3710 diffractometer
161 (measuring interval 5-120° 2Θ in 0.2° increments, measuring time of 15 s per step). The Bruker
162 EVA 2013 software with its database was used for the preliminary phase identification, then
163 Rietveld refinements using the Bruker program TOPAS3 were performed to confirm expected
164 lattice parameter shifts and the mono-phase character of the solid solutions.

165

166 **Single crystal X-ray diffraction**

167 Hand-picked single crystals suitable for X-ray diffraction measurements were obtained by
168 crushing crystal aggregates and choosing fragments with homogeneous extinction under crossed

polars. The crystal structures of ten representatives of the $Mg_{1-x}Fe_xSO_4 \cdot H_2O$ solid solution series, including the szomolnokite endmember, were determined from single-crystal X-ray diffraction data, measured at 295 K with graphite-monochromatized MoKα-radiation on a Nonius Kappa CCD diffractometer equipped with a 0.3 mm monocapillary X-ray optics collimator. Complete Ewald spheres up to 2θ = 80° were each collected in several sets of φ- and ω-scans with 2° rotation per CCD frame, at a crystal to detector distance of 30 mm. The integration and correction of the intensity data, including an absorption correction by multi-frame scaling and the refinement of lattice parameters, were done with the program DENZO-SMN (Nonius 1998).

Temperature-dependent X-ray data collections of the kieserite and szomolnokite endmembers were performed between +40 and –160 °C in steps of 40 K on a Bruker ApexII diffractometer equipped with a CCD area detector and an Incoatec Microfocus Source IμS (30 W, multilayer mirror, Mo-Kα), in a dry stream of nitrogen (Cryostream 800, Oxford Cryosystems). Several sets of φ- and ω-scans with 2° scan width were measured at a crystal-detector distance of 40 mm up to 80° 2θ full sphere. Absorption was corrected by evaluation of multi-scans. For the sake of data consistency, the lattice parameters extracted from the ApexII temperature-dependent measurements were corrected in such a way that their interpolated values at 20 °C match those obtained from the Nonius Kappa CCD room temperature measurements of the very same two endmember crystals.

All structure refinements were performed on F^2 with SHELXL-97 (Sheldrick 2008) in the 'traditional' non-reduced kieserite cell setting. Scattering curves for neutral atoms were used. The Mg/Fe ratios of the particular single crystals studied were extracted as a refined variable in the respective structure refinement runs.

CIF data for room temperature structures included in Tables 2 and 3 (plus CIF of endmember kieserite from Bechtold and Wildner 2016) and of all temperature-dependent structure investigations have been deposited with the submission at the MSA website.

IR spectroscopy

A part of each sample batch in powdered form and beforehand characterized by wet-chemical and powder X-ray diffraction analyses (see above) was used to conduct FTIR measurements in transmission, ATR (Attenuated Total Reflectance) and DRIFT (Diffuse Reflectance Infrared Fourier Transform) modes by means of the Bruker Tensor 27 FTIR spectrometer (Globar light source, KBr beam splitter, DTGS detector). For transmission measurements, the sample material was diluted in KBr at a weight ratio of 1:300 and pressed into pellets in a vacuum press. ATR measurements were done using the mountable Bruker ATR unit by pressing the sample powder against the diamond surface. For DRIFT measurements, the powder was pressed into the sample holder of a Perkin–Elmer DRIFT unit. Finely ground MgO was used as the reflectivity standard for the background measurements. All reflectance data were corrected via the Kubelka-Munk equation implemented in the Bruker OPUS software. The full wavenumber range (7000–400 cm^{-1}) was investigated in all analytical modes with a spectral resolution of 4 cm^{-1} (2 cm^{-1} spectral sampling). Each spectrum was averaged from 50 scans to reduce noise. For the DRIFT analyses, each sample was measured in pure state, as well as diluted with KBr in a ratio of 1:20, to enhance the absorption contribution to the resulting spectrum.

Low-temperature FTIR transmission measurements were done using a Linkam FTIR600 cooling stage equipped with KBr windows. KBr micropellets (2 mm diameter, sample dilution ratio 1:300) with the material pressed into the aperture of a steel gasket were used for these investigations. The metal gasket along with the small sample volume ensured easy handling and

swift thermal conductivity between the Ag-block of the cooling stage and the sample. Measurements were done in 40 K intervals ranging from 313 K (40 °C) down to 113 K (–160 °C). Some additional measurements at 93 K (–180 °C) could be done occasionally.

Raman spectroscopy

Raman spectra were measured on a Horiba Jobin Yvon LabRam–HR spectrometer, equipped with an Olympus BX41 optical microscope. A diffraction grating with 1800 grooves/mm and the 633 nm laser were used. The system is equipped with a Si-based, Peltier-cooled charge-coupled device (CCD) detector. A 100× objective (NA = 0.55) was selected for all room-temperature measurements. The wavenumber accuracy was better than 0.5 cm^{-1}, and the spectral resolution was determined to be ~0.3 cm^{-1}. The room-temperature Raman spectra were acquired between 100–4000 cm^{-1} shift, using multi-window scans with a counting time of 50 s per window and repeating every scan twice to eliminate spikes.

Low-temperature Raman measurements were conducted using the Linkam FTIR 600 cooling stage. Single crystals were placed on the Ag-block covered with a thermal conducting fluid. The use of single crystals instead of powdered material was essential, despite the inherent problems due to varying and unknown crystal orientation, as only single-crystal material allowed short-enough measuring times to prevent excessive ice buildup on the sample surface. The bulky stage necessitated the use of a long-distance 50× objective, with otherwise the same setup of the Raman instrument. The spectra were acquired in two separate spectral regions, i.e., 100–1600 and 2800–4000 cm^{-1} shift, with 5 s measuring time per window. Most acquisition temperatures match those of the FTIR low-temperature measurements to allow for direct comparison.

Band positions for both FTIR and Raman spectra were obtained by fitting the spectra in the program Peakfit (version 4.0). A Voigt-shaped band profile (i.e., a convolution of Gaussian and Lorentzian shapes) was used in both cases. Initial estimates of the number of bands and their distribution in IR and Raman spectra were based on the investigations on kieserite by previous authors (Stoilova and Lutz 1998; Lane 2007; Lane et al. 2015 for FTIR spectroscopy; and Chio et al. 2007 and citations therein for Raman spectra).

UV-Vis-NIR spectroscopy and crystal field calculations

An unpolarized optical absorption spectrum of a single crystal of $FeSO_4 \cdot H_2O$ was measured at room temperature in the spectral range 30000–3500 cm^{-1} on a mirror-optics microscope IRscope-II, attached to a Bruker IFS66v/S FTIR spectrometer. Appropriate combinations of light sources (Xe- or W-lamp, Globar), beam splitters (quartz, KBr) and detectors (GaP-, Si-, Ge-diodes, MCT) were used to cover the spectral range. The final spectrum is combined from four partial spectra (range in cm^{-1} / spectral resolution in cm^{-1} / averaged scans: UV: 30000–19380 / 40 / 1024; Vis: 19380–9700 / 20 / 1024; NIR: 9700–5260 / 10 / 768; IR: 5260–3000 / 4 / 512), which were aligned in absorbance for perfect match, if necessary, and then converted to the linear absorption coefficient α.

Crystal field (CF) calculations were performed in the framework of the semi-empirical Superposition Model (SM) of crystal fields using the HCFLDN2 module of the computer program package by Y.Y. Yeung (Chang et al. 1994). Due to the small number of observed crystal field levels, the power-law exponents t_k were fixed at their respective ideal electrostatic values, i.e., $t_4 = 5$ and $t_2 = 3$, and the Racah parameters were constrained to the ratio Racah C/B = 4.3 given in Figgis and Hitchman (2000). The reference metal–ligand distance R_0 was set to 2.13 Å, the mean <Fe–O> bond length in szomolnokite. For further details concerning the calculation

262 procedures the reader is referred to similar cases in Wildner et al. (2013) and respective
263 references therein.
264
265 **Results**
266
267 **Sample chemistry and powder X-ray diffraction**
268 The wet chemical analyses ensured precise knowledge of the actual Mg/Fe ratio in the bulk
269 synthesized products in their respective final state, i.e., after the purification process described in
270 the Experimental section. In addition, they revealed systematic differences between the pre-
271 adjusted and the actual Mg/Fe ratio in the product. The redox buffer greatly influences the extent
272 of discrepancy between theoretical $x_{Fe(preset)}$ and experimental $x_{Fe(sample)}$ values. Whereas the
273 crystals are usually clearly enriched in Fe when using the metallic Fe-foil as redox buffer,
274 preferential incorporation of Fe into the monohydrated sulfate is of much lesser extent with the
275 H_2SO_3 buffer in use. For the spectroscopic measurements, only batches with $| x_{Fe(sample)} - x_{Fe(preset)} |$
276 ≤ 0.06 as listed in Table 1 and shown in Fig. 1 were used.
277 Powder X-ray diffraction measurements and Rietveld refinements revealed the various
278 batches to consist nearly exclusively of kieserite-type $(Mg,Fe)SO_4 \cdot H_2O$ with occasional traces of
279 hexahydrite or rhomboclase. The patterns showed no signs of Bragg peak splitting or suspicious
280 broadening, thus confirming compositional homogeneity and the mono-phase character of the
281 obtained monohydrate sulfate solid solutions.
282 As noted already above, the Mg/Fe ratios of the crystals hand-picked for single crystal
283 X-ray diffraction studies were extracted as a refined variable in the structure refinements.
284
285 **Crystal structures**

The present single crystal X-ray measurements and structure refinements along the kieserite–szomolnokite solid solution series, $Mg_{1-x}Fe_xSO_4 \cdot H_2O$, gave no indications of octahedral Mg/Fe cation ordering, domain formation or related effects. Crystal data, details of the data collections and structure refinements of four selected representatives including szomolnokite are listed in Table 2, respective final atomic coordinates and displacement parameters in Table 3. Corresponding temperature-dependent data of the endmembers kieserite and szomolnokite are compiled for two selected temperatures in Tables 4 and 5. Important crystal chemical data at ambient and temperature-dependent conditions are given in Tables 6 and 7, respectively. Details for the kieserite endmember at room temperature were recently reported by Bechtold and Wildner (2016) in their structural study of the kieserite–cobaltkieserite solid solution series, and are included in Tables 2 and 6 for convenient comparison.

The kieserite structure type is built from kinked chains of O3($\equiv H_2O$)-corner-sharing $MgO_4(H_2O)_2$ octahedra, elongated along their O3–O3 axis, and nearly regular SO_4 tetrahedra, intra-linking adjacent octahedra within the chains by common O2 corners. These octahedral-tetrahedral chains are aligned parallel to the *c* axis and linked to a framework structure by sharing the remaining polyhedral O1 corners as well as by moderately strong O3···O2 hydrogen bonds.

The structural behavior of the $Mg_{1-x}Fe_xSO_4 \cdot H_2O$ kieserite–szomolnokite solid solution series is illustrated in Figures 2–5. It is evident that complete miscibility exists and that the series shows Vegard-type behavior, with all lattice parameters (Fig. 2) changing in a linear way across the entire composition. The cell volume V (+10 Å^3), angle β (+0.6°), and the lattice parameters *a* and *c* (+0.18 and 0.14 Å) increase with Fe uptake, only the *b* axis (–0.08 Å) shows an opposite trend. The clear increase of individual and average Me–O bond lengths and of the octahedral volume (Figs. 3a and 4a) comply with the larger ionic radius of Fe^{2+} compared to Mg. The comparatively moderate increase of the Me–O2 bond can be partly related with the shortening of

the *b* axis, since Me–O1, –O2 and –O3 bonds have their major vector components parallel to the crystallographic *a*, *b* and *c* axis, respectively. With Fe uptake, also the octahedral distortion increases for bond lengths as well as bond angles (Figs. 3ab, Table 6), and the octahedral shape changes from a clear [4+2] coordination in kieserite towards a [2+2+2]-type coordination in szomolnokite. Also the tetrahedral SO_4 group slightly expands with increasing Fe content (Figs. 3c, 4a), but bond length and also angular changes (Fig. 3d) hardly exceed a 3σ limit. The medium-strength hydrogen bond O3–H···O2 lengthens only slightly (Fig. 4c), despite having its main component parallel to the strongly increasing *a* axis.

The prominent changes within the MeO_6 octahedron along the $Mg_{1-x}Fe_xSO_4 \cdot H_2O$ solid solution are accompanied by mutual compensating polyhedral rotations and tiltings, evidenced by a significant decrease of the Me–O–S and Me–O3–Me angles shown in Fig. 4b. Hence, the tilting within the octahedral chain increases and the rather rigid SO_4 tetrahedron rotates by up to 2.3° (O1–O1' edge; O2–O2' edge: 2.0°) around its twofold axis (Fig. 5); combined with the strong change of the octahedral O1–Me–O3 angle this leads to a mutual shift of the polyhedral chains along the *c* axis, resulting in the increase of the cell angle *β* and especially of the *a* axis.

When temperature is reduced, some structural properties of the kieserite and szomolnokite endmembers seem to deviate more or less from a linear response. As expected, the cell volumes decrease, as well as *β*, *a*, and *c*, but the *b* axis lengthens for both compounds (Fig. 6). Also the mean Me–O bond lengths (Fig. 7a) and octahedral volumes (Fig. 7c) decrease, mainly by reducing the longest Me–O3 bond; the only other Me–O change larger than 3σ across the whole temperature range is a further slight shortening of shortest Fe–O2 bond; thus, for the FeO_6 octahedron the tendency towards a [2+2+2] coordination still increases. Most acute octahedral bond angles marginally increase (Fig. 7b), thus slightly reducing bond angle distortion at lower temperatures. If S–O bond lengths are not corrected for thermal motion, the apparent increase in

S–O bond lengths and tetrahedral volume upon cooling (Fig. 7cd) has to be assigned as the respective artifact. Applying a 'simple rigid bond' correction according to Downs et al. (1992) results (apart from a generally inherent distance increase) in a practically constant <S–O> bond length in kieserite and a marginally decreasing one ($\Delta_{<S–O>}$ = –0.0014 Å) in szomolnokite upon cooling along the full temperature range. The tetrahedral angles show divergent trends with temperature reduction (with maximal changes of 0.3°), i.e., tending to lower distortion in kieserite compared to higher distortion in szomolnokite. The O3–H···O2 hydrogen bond length consistently shortens in both compounds by ~0.028 Å within the investigated 200 K range (Fig. 8a). Also corresponding polyhedra-linking angles show parallel behavior in kieserite and szomolnokite (Fig. 8b): the octahedral chain angle Me–O3–Me remains constant, but Me–O–S angles get smaller by 1.1° (O2) and ~0.7° (O1). The resulting rotation of the SO_4 tetrahedron upon cooling has the same sense as found for increasing x_{Fe} in the solid solution (compare Fig. 5); between room temperature and –160 °C it amounts to roughly 1.1° for both O1–O1' and O2–O2' tetrahedral edges in both endmembers.

IR spectra

The IR spectra of the Mg/Fe monohydrated sulfates feature several clearly discernible absorption phenomena (Fig. 9). Taking as an example the FTIR spectra measured in transmission mode, the H_2O absorption region is dominated by a prominent band at 3182–3245 cm^{-1} (3.14–3.08 μm), representing the symmetric stretching vibration $\nu_{1(H_2O)}$ of the H_2O molecule. A poorly resolved broad shoulder at even higher wavenumbers (3367–3391 cm^{-1} / 2.97–2.95 μm) represents $\nu_{3(H_2O)}$, the antisymmetric H_2O stretching mode. The H_2O bending vibration $\nu_{2(H_2O)}$ occurs at 1525–1496 cm^{-1} (6.56–6.68 μm). A major band group (centered around 1150 cm^{-1} / 8.70 μm) corresponds to the antisymmetric $\nu_{3(SO_4)}$ stretching mode of the sulfate tetrahedra and

the IR-forbidden symmetric stretching mode $\nu_{1(SO_4)}$, visible as a weak but well-defined band around 1025 cm^{-1}. A pronounced absorption phenomenon (hereafter labeled 'Peak 850 cm^{-1}'), considered as a potential diagnostic feature for monohydrated kieserite-group sulfates by Lane (2007), occurs in our data (Fig. 9) at 884–831 cm^{-1} (11.31–12.03 μm). Lastly, a band group at 630 cm^{-1} (15.87 μm) is assigned to the $\nu_{4(SO_4)}$ bending modes.

It should be mentioned that the absorption band shape and even position vary significantly between individual FTIR measuring modes (Fig. 9). Nevertheless, the overall spectral appearance is comparable, with the absorption of the H_2O bending vibration $\nu_{2(H_2O)}$ being enhanced in DRIFT spectra when using diluted sample material (Fig. 9). The sole exceptions as to the consistency of the spectral shapes are DRIFT measurements on pure sample material (no KBr dilution), where most intrinsic absorption phenomena at lower wavenumbers are suppressed, with strong artifacts present, such as the 'reststrahlenband' labeled 'R' in Fig. 9, a pronounced absorption at around 1300 cm^{-1}. Absorptions due to H_2O modes at high wavenumbers are noisy, leading to the loss of resolution between the $\nu_{1(H_2O)}$ and $\nu_{3(H_2O)}$ bands. The spectral position of the reststrahlenband artifact, however, is also dependent on the sample composition, shifting from 1360 to 1283 cm^{-1} (7.35 to 7.78 μm) from kieserite to szomolnokite.

A specific benefit of DRIFT measurements, however, is the enhanced amplitude of absorption bands assigned to H_2O combination modes in the 4400–5200 cm^{-1} (2.27–1.92 μm) spectral region. Three distinct bands occur at 4688, 4845 and 5087 cm^{-1} (2.13, 2.06 and 1.97 μm, respectively) in endmember kieserite. When x_{Fe} increases, both peripheral bands converge closer to the central one at 4845 cm^{-1} (2.06 μm), creating the misleading impression (mainly in case of poor resolution or enhanced spectral noise) of a dominant single broad band at 4750 cm^{-1} (2.10 μm) with a weaker one at 5025 cm^{-1} (1.99 μm) in szomolnokite (Fig. 10ab, Table 8).

In agreement with the structural behavior along the (Mg,Fe)$SO_4 \cdot H_2O$ solid solution series reported above, the positional changes of the IR absorption bands with increasing Fe content also show linear trends within limits of error (Fig. 11). The only exceptions to this rule are the above-mentioned H_2O combination modes seen in DRIFT spectra, where a more complex trend is observed. In many cases, the changes are quite subtle, such as for the position of the SO_4 vibrations and that of the H_2O bending mode, where the decrease in wavenumber from the kieserite to the szomolnokite endmember amounts to a mere 30 cm^{-1} in all three measuring modes. Clearer correlation trends can be observed for the H_2O stretching vibrations, where the well-resolved $\nu_{1(H_2O)}$ band changes in position from 3182 in kieserite to 3245 cm^{-1} in szomolnokite. A somewhat smaller but still significant change can be seen for the apparent monohydrate sulfate diagnostic 'Peak 850 cm^{-1}' (Lane 2007; Lane et al. 2015) that shifts in our data from 884 in kieserite to 831 cm^{-1} with increasing x_{Fe}. No significant correlation could be observed for the $\nu_{3(H_2O)}$ band position, due to it being present as a mere shoulder of the afore-mentioned $\nu_{1(H_2O)}$ vibration, leading to significant fitting errors. The variations in the wavenumber position of relevant spectral absorption phenomena for the individual measurement modes, as well as the respective linear regression coefficients, are summarized in Table 8.

From the acquired temperature-dependent FTIR-spectra between +40 and –160/180 °C (Fig. 12), two behaviors are evident. Firstly, the sulfate tetrahedra behave as a rigid unit, which is reflected by the nearly stable position of all SO_4^{2-} vibrational modes regardless of temperature. On the contrary, the H_2O-related symmetric stretching vibration in kieserite shows a significant decrease in wavenumber by 29 cm^{-1} (0.030 μm) from +40 °C down to –160 °C at a rate of –0.145 cm^{-1}/°C, and szomolnokite, measured down to –180 °C, shows a change of 33 cm^{-1} (0.022 μm) with a comparable rate of –0.150 cm^{-1}/°C. The rate of decrease appears to be constant, independent of the Mg/Fe ratio (Fig. 12). The diagnostic 'Peak 850 cm^{-1}' discussed earlier shows

a wavenumber increase upon cooling, whereas the H_2O bending vibration remains nearly unaffected by the temperature change.

Raman spectra

The changes in Raman band position along the kieserite–szomolnokite solid solution are also linear as could be expected from the FTIR results (Table 9). Figure 13 graphically depicts the positional changes of prominent bands across the solid solution series in detail, and Table 9 gives the respective coefficients of the linear regression between the band position and x_{Fe}.

The Raman spectra consist of numerous narrow bands in the 100–1600 cm^{-1} shift region, with much better resolution compared to FTIR spectra (Fig. 9 vs. 14a). The most prominent band is the symmetric stretching vibration $\nu_{1(SO_4)}$ of the sulfate tetrahedron with Raman shift at 1042 cm^{-1} for kieserite and 1018 cm^{-1} for szomolnokite. Several relevant spectral features occur at lower shift values, and the most prominent are located at ~270, ~430 and a doublet at ~620 cm^{-1}. Weak bands in the spectral range 1100–1600 cm^{-1} are assigned to the split $\nu_{3(SO_4)}$ vibrations (Stoilova and Lutz 1998; Chio et al. 2007), with the exception of the broader H_2O bending mode at 1500 cm^{-1}. Stretching vibrations of the H_2O molecule occur in the expected region, i.e., the $\nu_{1(H_2O)}$ band is located at 3179 up to 3247 cm^{-1} with increasing x_{Fe} (Fig. 14b), whereas the antisymmetric $\nu_{3(H_2O)}$ mode is again present as its shoulder, analogous to the FTIR spectra.

It should be mentioned that despite the sample being in finely powdered form, the effect of varying (and unknown) crystallite orientation, influencing the relative amplitude of the Raman bands, is clearly visible. This is attributed to the small scattering volume excited by the laser spot in comparison with the much higher (and thus orientation-averaging) sample volume measured by IR spectroscopic techniques (in the order of mm^3, depending on the specific measuring mode). Fortunately, only band amplitudes are affected, while their positions remain the same.

Low-temperature Raman measurements have also been conducted. As expected, a significant composition-independent systematic shift of the band position with temperature is seen for the $\nu_{1(H_2O)}$ band, which decreases in wavenumber shift by about 30 cm^{-1} across the full temperature range, and represents the strongest change among all examined bands. The $\nu_{3(H_2O)}$ band is again poorly resolved, thus impeding any precise fit. The very good band resolution and low FWHM of the SO_4 vibrational bands in Raman spectra allow accurate examination of even their subtle positional changes, which are not so apparent in IR spectra (Table 9). In general, their wavenumber change with temperature never exceeds 10 cm^{-1} within the examined temperature range (Table 9). A systematic increase in wavenumber shift is observed at low temperature for the lowest-energetic bands, representing octahedral stretching modes according to Chio et al. (2007). For all observed bands, the rates at which the band positions change with temperature remain constant across the examined temperature range, allowing one to determine a mean shift per 1 °C for the individual bands, included in Table 9.

UV-Vis-NIR spectroscopy and crystal field calculations

The optical absorption spectrum of szomolnokite is shown in Fig. 15. Two prominent crystal field absorption bands centered around 7650 and 10640 cm^{-1} are attributed to transitions from the $^5T_{2g}$ ground state with parental ^5D term to the spin-allowed $^5E_g(D)$ level of octahedral Fe^{2+}, which is split into two non-degenerate states in non-cubic crystal fields (i.e., in a pseudo-tetragonal approach $^5A_{1g}$ and $^5B_{1g}$). A sharp peak at 6565 cm^{-1} within the low-energy wing of the first crystal field band represents the first overtone of the O–H stretching mode. All other spectral features observed between 19800 to 25900 cm^{-1} (see inset in Fig. 15) are very weak and can be attributed to spin-forbidden crystal field transitions of Fe^{2+} derived from excited triplet terms, very probably $^3T_{1g}(H)$, $^3T_{2g}(G)$, $^3E_g(H)$, $^3T_{1g}(G)$ and $^3T_{2g}(F2)$, in sequence of increasing energy

(labels for cubic symmetry). The background increase in absorption towards the UV is most likely related to the LMCT transition (ligand–metal charge transfer) of trace contents of Fe^{3+}, causing the light beige hue of szomolnokite. The crystal field (CF) calculations, either based on a full superposition model (SM) calculation in the actual triclinic polyhedral symmetry, or on a pseudotetragonal approach assuming a [4+2]-elongated octahedron and employing classical CF parameters, both yield basically comparable and reasonable results, summarized in Table 10. They also match well with respective results for cobaltkieserite (Wildner 1996), showing the comparability of crystal fields in transition metal kieserite-group compounds. Apart from similar field strengths Dq_{cub} and Racah parameters, even the tetragonal distortion parameter Dt, expressing the polyhedral elongation of the H_2O–Me–OH_2 axis, is similarly underestimated due to the higher field strength of H_2O molecules compared to oxygen ligands of the SO_4 groups.

Discussion

Crystal structural evolution and crystal chemistry

In view of previous single-crystal structure investigations of endmember kieserite (Bechtold and Wildner 2016; earlier Hawthorne et al. 1987) and szomolnokite (Wildner and Giester 1991), the solid solution series presented here behaves as expected: in particular, all lattice parameters and crystal chemical data exhibit Vegard-type behavior within the limits of error, i.e., they show linear changes with Mg/Fe ratio. The extent of those changes along the solid solution allows, amongst others, to infer the Mg/Fe ratio in $Mg_{1-x}Fe_xSO_4 \cdot H_2O$ samples of unknown composition from X-ray data. Furthermore, this work also constitutes an important basis for any further theoretical calculations of interest, as well as the possibility to easily determine the values of thermodynamic parameters for any member of the solid solution. This is

enabled because the Vegard-type behavior indicates one-site ideal mixing of both endmembers (Powell and Holland 1993). Enthalpy, entropy, molar volume, as well as heat capacity and thermal expansion can be determined by the linear combination of these parameters for both endmembers in their respective formula ratio in the sample (van Hinsberg et al. 2005a,b).

As expected from a crystal chemical point of view, the replacement of the smaller Mg cation (r_{Mg} = 0.720 Å) by the larger Fe^{2+} ($r_{Fe^{2+}}$ = 0.780 Å; all radii from Shannon 1976) leads to a corresponding increase of average and individual Me–O bond lengths, of the respective octahedral volume, and hence also of the unit-cell volume (Figs. 2b, 3a and 4a). However, a more detailed analysis is advisable, since this is not the case for the kieserite-cobaltkieserite solid solution series, $Mg_{1-x}Co_xSO_4 \cdot H_2O$, recently studied by Bechtold and Wildner (2016). There, the replacement of the smaller Mg by the larger Co^{2+} ($r_{Co^{2+}}$ = 0.745 Å) leads to an increase of average and individual Me–O bond lengths and of the octahedral volume, but surprisingly at the same time the cell volume is reduced. Apart from Bechtold and Wildner (2016) (and earlier Wildner and Giester 1991 and Giester and Wildner 1992) for kieserite-type compounds, a comparable aberrant behavior has been explicitly noted and documented for blödite-type compounds $Na_2Me^{2+}(SO_4)_2 \cdot 4H_2O$ (Stoilova and Wildner 2004) or for Tutton's salts $K_2Me^{2+}(SO4)_2(SO_4)_2 \cdot 6H_2O$ (Bosi et al. 2009). Bechtold and Wildner (2016) attribute this mismatch to the absence of (for Mg) and the presence of (for Co^{2+}) 3*d* orbitals, the latter imposing anisotropy of the electron density around transition metal (TM) cations. This anisotropy affects the position of the bond critical point $\mathbf{r}_c$ along the Me–O bond path and the electron density $\rho(\mathbf{r}_c)$ at this point (cf. e.g., Bader 1998). For Mg–O bonds, $\mathbf{r}_c$ lies comparatively closer to Mg with lower $\rho(\mathbf{r}_c)$ than for 3*d*TM–O bonds, thus in turn also affecting the electron density at the oxygen ligands and hence the second coordination sphere: S–O bond lengths (slightly) increase with Co- and in the present case Fe-uptake (Fig. 3c); however, the second coordination

sphere 'contracts' due to increased interpolyhedral folding as evidenced by reduction of the Me–O–S and Me–O–Me angles shown in Fig. 4b (also see respective discussion, Figures and references in Bechtold and Wildner 2016). These aspects are also directly related to significant differences in the total, as well as Me^{2+}-cation polarizabilities α in kieserite compared to the 3*d*TM kieserite-group compounds, as recently discussed by Gagné et al. (2018) for various structure types comprising Mg- and 3*d*TM-representatives. All the arguments discussed for Co^{2+} also hold for Fe^{2+} compared to Mg, but due to the clearly higher difference in ionic radii, no eye-catching volume mismatch is found for the present kieserite–szomolnokite solid solution series.

Nonetheless, szomolnokite (and Fe-rich representatives in general) also deviates in some aspects from the otherwise uniform properties of kieserite and the 3*d*TM-kieserite-group sulfates, especially concerning the tendency towards a [2+2+2]-coordination in the octahedral unit, compared to clear [4+2] geometries in the kieserite-group monohydrate sulfates of Mg, Mn, Ni, Co and Zn (see Fig. 2 in Wildner and Giester 1991). Hence we may suppose that a moderately elongated octahedral [4+2]-environment complies well with packing requirements of the kieserite structure type (note that a strong elongation imposed e.g., by Jahn-Teller affected Cu^{2+} is not accepted, leading to symmetry reduction; Giester 1988). The deviation observed for szomolnokite might be attributed to the uneven *d*-electron distribution of high-spin $3d^6$-configurated Fe^{2+}, with one excess (i.e., paired) electron in the triply degenerate t_{2g} set of the 3*d* orbitals. Other representatives have either no (for Mg), symmetrically (for Mn^{2+}, Ni^{2+}) or fully occupied (for Zn^{2+}) 3*d* orbitals, or two excess (paired) electrons in the t_{2g} orbital set (as for Co^{2+}). In the latter case, an appropriately elongated [4+2] Jahn-Teller distortion is in theory expected, neglecting any thermodynamic considerations (in practice, respective static effects are not statistically detectable in room temperature crystal structures; Wildner 1992). However, in case of $3d^6$-configurated Fe^{2+}, a compressed octahedral [2+4] Jahn-Teller distortion is theoretically predicted, thus

525 suggesting the specific uneven *d*-electron distribution as probable explanation for the particular
526 deviation of the octahedral distortion in szomolnokite (but there seem to exist no systematic
527 studies seeking to generally verify a respective static effect for Fe^{2+}).
528
529 **IR, Raman and crystal field spectra**
530 **IR spectra at ambient conditions.** The linear Vegard-type behavior observed in the
531 structural data of the $Mg_{1-x}Fe_xSO_4 \cdot H_2O$ solid solution series (Figs. 2–4) is also reflected in the
532 results of FTIR and Raman spectroscopic measurements. With wavenumber units in use, one can
533 recognize a linear change of the position of IR spectral bands across the kieserite–szomolnokite
534 series (Fig. 11, Table 8). Evidently, the wavenumber of the prominent symmetric stretching
535 vibration $\nu_{1(H_2O)}$ of the H_2O molecule increases with Fe content. This is in agreement with the
536 structural data (Fig 4c, Table 6), where the O3···O2 donor–acceptor hydrogen bond length
537 increases with x_{Fe}, expectably leading to the observed band behavior (e.g., Libowitzky 1999).
538 Likewise, a similar blue-shift of the antisymmetric stretching mode $\nu_{3(H_2O)}$ would also be
539 expected. However, since the band overlaps significantly with the prominent $\nu_{1(H_2O)}$ absorption,
540 the trend is obscured due to reduced fitting accuracy. The H_2O bending mode $\nu_{2(H_2O)}$ decreases
541 slightly but constantly in position with increasing x_{Fe}, which might be correlated with the
542 widening of the acceptor–donor–acceptor angle O2···O3···O2 from kieserite to szomolnokite
543 (136.7–140.5°). Both the symmetric $\nu_{1(SO_4)}$ vibration and the three bands assigned to the split
544 $\nu_{3(SO_4)}$ mode (Chio et al. 2007; Lane 2007) decrease in wavenumber with increasing x_{Fe}, in accord
545 with the observed slight relaxation of the SO_4^{2-} tetrahedron towards szomolnokite (Figs. 3c, 4a,
546 Table 6). Of the latter three bands, only the major one is depicted and its position followed in Fig.
547 11 and Table 8, since the peripheral bands present as shoulders are not traceable reliably. Similar
548 to $\nu_{1(H_2O)}$, the prominent 'Peak 850 cm^{-1}' absorption band deemed as diagnostic by Lane (2007)

549 and Lane et al. (2015) could also be used to infer the Mg/Fe ratio, since it shows a rather
550 pronounced wavenumber decrease towards Fe-rich compositions (i.e., 831 cm^{-1} in szomolnokite).
551 A group of bands at ~630 cm^{-1}, assigned by Lane et al. (2015) to the $\nu_{4(SO_4)}$ vibration, cannot
552 easily be exploited for cosmochemical considerations, as the spectral region not only consists of
553 numerous bands with varying FWHM, but also does not prove to be clearly discernible from the
554 signals of other sulfates and even silicates. Furthermore, the Martian atmosphere is dominated by
555 CO_2 that has a strong band centered at ~667 cm^{-1}, potentially obscuring bands within the wings of
556 the CO_2 band (~529 to 794 cm^{-1}; e.g., Christensen et al. 2000). Therefore, the IR spectral region
557 between 700 and 300 cm^{-1} (14.3–27.0 μm) was not studied in further detail.
558 Contrary, the 4400–5200 cm^{-1} (2.27–1.92 μm) spectral region, where absorptions
559 associated with combination modes of the H_2O stretching and bending modes occur, is
560 considered by many authors to be an important spectral feature in reflectance spectra from Mars
561 orbiters, allowing not only to discern kieserite from other sulfate hydrates, in which the
562 prominent bands occur at higher wavenumbers (Mangold et al. 2008; Noel et al. 2015), but also
563 to roughly infer its Fe content (Cloutis et al. 2006; Bishop et al. 2009; Liu et al. 2016). The H_2O
564 combination modes are most apparent in DRIFT spectra of pure undiluted sample material. The
565 kieserite endmember shows a typical set of three bands at ~4700, 4850 and 5090 cm^{-1} (2.13, 2.06,
566 1.96 μm) (Fig. 10ab, Table 8). A comparison between the kieserite and szomolnokite endmember
567 patterns (Bishop et al. 2009) has led many of the above-mentioned authors to infer the presence
568 of a single dominant absorption band (2.09 μm) with a shoulder in szomolnokite, instead of the
569 clearly visible triplet observed in kieserite. As can be seen in Fig. 10a, all three bands occur in
570 szomolnokite as well, with the peripheral bands ‘converged’ in their position closer to the central
571 one. Given their broad FWHM, the three bands, shifted close together in szomolnokite, create the
572 misleading impression of a broad peak (central band) with a single shoulder (highest-energetic

peak) with the center at a higher wavenumber than the strongest of the three individual bands discernible in endmember kieserite, which corresponds to the lowest-energetic peak in the triplet (Fig. 10a, Table 8). A more detailed analysis of the behavior of the triplet with increasing x_{Fe} revealed a non-linear relation of the band position with the Mg/Fe ratio at higher Fe contents. This discrepancy may, however, be attributed to the presence of a weak yet broad band caused by Fe^{2+} crystal field transitions (Fig. 15), which partly alters the background even in the H_2O combination mode region due to its large FWHM (Jamieson et al., 2014). Together with the H_2O-related combination bands being very weak even when measuring undiluted sample material in DRIFT mode, a fitting error is introduced, which, to our opinion, accounts for the non-linearity of the observed trends when higher amounts of Fe^{2+} are present (Fig. 10b, Table 8).

As noted above, the wavenumber of any particular absorption in the IR spectrum also changes in relation to the measuring technique (Table 8). As an example, the $\nu_{1(H_2O)}$ band occurs at 3182 cm^{-1} in endmember kieserite measured in transmission mode, whereas the corresponding feature is centered at 3165 cm^{-1} in ATR mode and as high as 3203 cm^{-1} using the DRIFT technique on the very same sample (3.14, 3.16 and 3.12 μm, respectively). The shift in band position is to be attributed to the known change in refractive index close to a spectral absorption, dependent on the ratio of the reflection and transmission components constituting the final spectral signal. Besides, DRIFT spectra of undiluted sample material show significant artifacts (reststrahlenband, etc.) instead of the expected sulfate vibrations between 1300 and 370 cm^{-1} (7.69 and 27.02 μm). A sample dilution of 1:20 in an IR-transparent material (KBr) already leads to a spectral shape very close to the result of proper transmission measurements, with enhanced amplitudes of weaker bands, such as $\nu_{2(H_2O)}$ and the H_2O combination modes.

All these factors have implications for measurements on Mars, where IR spectra reflected by 'fluffy' kieserite aggregates (more transmission) would somewhat differ in shape and band

position from signals acquired on compact kieserite masses or crusts due to the different reflection/transmission ratio of the particular material. Disregard of these issues could be misleading in the assessment of the properties and composition of the measured monohydrate sulfate. Contrary, the grain size seems to have little effect on the band *position* in IR reflectance spectra (Jamieson et al. 2014; Pitman et al. 2014).

With this in mind, promising spectral features for a semi-quantitative assessment of the chemistry of kieserite-group solid solutions from orbiter spectra should be the absorption bands with a pronounced regression slope in relation to x_{Fe}. In addition to the H_2O combination mode region centered at ~4900 cm^{-1} (2.04 μm), a promising candidate would seem to be the $\nu_{1(H_2O)}$ band, showing a wavenumber change towards higher values by ~60 cm^{-1} (0.06 μm) from kieserite to szomolnokite (Fig. 11). While $\nu_{2(H_2O)}$ and the sulfate modes all show smaller positional changes with respect to sample chemistry, the 'Peak 850 cm^{-1}' (11.8 μm), deemed as diagnostic for monohydrated sulfates by previous authors (Lane et al., 2015), appears to be promising as well due to a comparatively large shift in wavenumber of roughly 50 cm^{-1} (0.72 μm).

When expressing positions and shifts of the spectral bands (e.g., as done just above), a 'technical' issue immediately becomes apparent. The choice of spectral units, i.e., wavenumber in cm^{-1} vs. wavelength in μm, significantly influences the shape of the spectral envelope and the apparent extent of changes in the position of absorption features. Whereas the difference in the wavenumber position of the H_2O symmetric stretching mode $\nu_{1(H_2O)}$ and the 'Peak 850 cm^{-1}' band amounts to a comparable shift of 60 and 50 cm^{-1}, respectively, the same values expressed in wavelength as spectral unit amount to 0.06 and 0.72 μm, respectively, setting both values apart by an entire order of magnitude. While wavelength units are more commonly used in the Vis-NIR research of the cosmochemical community, wavenumber units were chosen for this work because it better suits our aim of comparing the structural and spectroscopic behavior of the

kieserite–szomolnokite solid solution series. Unlike wavelength, wavenumber units are directly proportional to the frequency and thus to the energy of the observed phonons, allowing for a meaningful comparison with structural data. Furthermore, IR spectra represented in wavenumber units facilitate band fitting using Voigt profiles, as the absorption bands appear symmetrical, unlike the situation with wavelength units (especially > 4 μm). In this way, we were able to amply demonstrate the linear Vegard-type dependency of vibrational bands on the interatomic distances and polyhedral size along the entire kieserite–szomolnokite solid solution and the consistency of single-crystal X-ray and spectral results. Furthermore, the direct comparison of related vibrational features between Raman and IR spectra is simplified. The corresponding wavelengths λ (in μm) can be easily obtained according to the formula $\lambda(\mu m) = 10000/\nu(cm^{-1})$.

Temperature dependence of IR spectra. Temperature-related spectral changes (Fig. 12) are important to consider, especially for interpreting extraterrestrial data, e.g., from Mars, where the average temperature spans from +20 to –120 °C (Witzke et al. 2007) and reaches values as low as 5 K elsewhere. Considering that the two bands showing the strongest change with increasing Fe content ($\nu_{1(H_2O)}$ and 'Peak 850 cm^{-1}') are also those showing the greatest variation in position with temperature (Fig. 12), the range of error in the assessment of x_{Fe} from a single band can be up to ±0.25 without the approximate knowledge of temperature. The same, considering the temperature sensitivity of the fundamental H_2O bands, will apply to their combination modes in the ~4900 cm^{-1} region (Fig. 10ab), which, according to the results for kieserite of Jamieson et al. (2014), split further apart with decreasing temperature. This behavior is in contrast to the 'merging' of the three bands from kieserite to szomolnokite into a seemingly single broad absorption at higher wavenumbers. In contrast to $\nu_{1(H_2O)}$, the H_2O bending vibration hardly changes with temperature, obviously related to the small change of the acceptor–donor–

acceptor angle O2···O3···O2 (~1.6°), compared to the significant influence of the Mg/Fe ratio (~4°)

As to the sulfate bands, the splitting of $\nu_{3(SO_4)}$ into three components and the low amplitude of the $\nu_{1(SO_4)}$ symmetric stretching vibration are the effects that hamper precise fitting and estimation of x_{Fe}, not temperature, towards which they are rather insensitive.

Raman spectra at ambient conditions. Raman spectra acquired across the solid solution also exhibit systematic band shifts with variable x_{Fe} (Figs. 13 and 14, Table 9), and corresponding vibrational modes show the same behavior in IR and Raman spectra. However, the better band resolution due to narrower FWHMs and fewer band overlaps in Raman spectra allow for a more precise refinement of the subtle changes in position and splitting of the diverse SO_4 modes, as well as a more accurate characterization of octahedral modes with changing Mg/Fe ratio.

The increase in hydrogen bond length with increasing x_{Fe} leads to the expected increase in the wavenumber of the H_2O symmetric stretching vibration from 3179 to 3247 cm^{-1} shift (3.14–3.08 μm). The nearly perfect match between the positions observed in the IR transmission spectra and the Raman data underline the consistency of both data sets.

The change in position of the $\nu_{1(SO_4)}$ vibration from 1042 to 1018 cm^{-1} between kieserite and szomolnokite, respectively, also parallels its behavior in the IR spectra, where it was present, albeit weak (e.g., Fig. 11; Lane 2007). On the contrary, it represents the strongest feature in the Raman spectra of the kieserite–szomolnokite solid solutions, making it the optimum candidate to infer the Mg/Fe ratio, more so given its stable position at lower temperatures (see below). Also the three well-resolved bands assigned to the split antisymmetric $\nu_{3(SO_4)}$ vibration offer a more accurate insight into the behavior of the sulfate tetrahedron, in that the spectral position of all three modes tends to decrease with increasing x_{Fe}, as noted before for other methods. The same

669 holds true for the wavenumber decrease of the other modes of the SO_4 group (Fig. 13, Table 9),
670 in accord with its slight relaxation upon Fe uptake revealed by the single-crystal diffraction data
671 (Fig. 3cd, Table 6). The bands observed in the 100–250 cm^{-1} shift region feature a component at
672 ~220 cm^{-1} assigned by Chio et al. (2007) to a vibration involving the translation along the Fe–
673 H_2O bond. However, its spectral position remains nearly unchanged regardless of the Mg/Fe ratio
674 (Fig. 13, Table 9), which challenges this assignment, given the variation in octahedral bond
675 lengths across the solid solution (Table 6). A significant positional decrease was observed for the
676 lowest mode at ~130 cm^{-1}, changing from 137 to 112 cm^{-1} from kieserite to szomolnokite. While
677 we are unable to ascertain the exact character of this vibration, its significant change with the
678 Mg/Fe ratio makes it another viable band to infer on the chemistry of kieserite-group minerals
679 from vibrational spectra.
680
681 **Temperature dependence of Raman spectra.** Band shifts in low-temperature Raman
682 spectra show similar behavior to that of the corresponding vibrational modes observed in the IR
683 spectra (Table 9). Better band resolution compared to IR spectra allows, however, to accurately
684 track even the subtle positional changes of sulfate-related peaks. The highest-energy peak of the
685 split $\nu_{3(SO_4)}$ mode at ~1200 cm^{-1} increases, while the lowest-energy $\nu_{3(SO_4)}$ peak at ~1100 cm^{-1}
686 decreases in position (Table 9). This increase of spectroscopic distortion may be correlated with
687 the slight increase in geometric tetrahedral distortion at reduced temperatures (compare
688 respective distortion parameters in Tables 6 and 7).
689 The vibrational mode at ~220 cm^{-1} shift shows a notable increase in wavenumber at low
690 temperature. This behavior, together with its position at ~220 cm^{-1}, implies a possibility that the
691 diagnostic 'Peak 850 cm^{-1}' absorption feature in the *IR spectra* (Lane et al. 2015), is actually a
692 combination of this mode and the $\nu_{4(SO_4)}$ mode at ~630 cm^{-1}, which decreases in wavenumber

693 from kieserite to szomolnokite. This would lead to the expected wavenumber decrease of the
694 resulting IR absorption at ~850 cm^{-1} from kieserite to szomolnokite, as would be dictated by the
695 trends seen for both $\nu_{4(SO_4)}$ components (Fig. 13). The absence of this band in the Raman spectra
696 supports this theory, since such phenomena are suppressed in Raman spectroscopy to a great
697 extent due to the different underlying physical process of spectrum formation (IR absorption
698 versus inelastic scattering). The splitting of the $\nu_{4(SO_4)}$ vibration into two bands may also account
699 for the slight asymmetry observed for the 'Peak 850 cm^{-1}' IR band (Fig. 13, Table 9).
700
701 **Use of vibrational spectra to infer the composition of Martian kieserite.** Linear trends,
702 observed for changes in structural parameters of $(Mg,Fe)SO_4 \cdot H_2O$ (Figs. 2-4), as well as in the
703 position of IR bands (when expressed in wavenumbers) and in Raman spectra, clearly correlate
704 with the Mg/Fe ratio (Figs. 11, 13). Aside from documenting in detail the behavior of kieserite-
705 group compounds throughout the Mg/Fe solid solution series, the linearity of the data also allows
706 its use as a standard in evaluating IR spectra acquired during orbiter missions as well as Raman
707 measurements, which will be conducted during future rover missions to Mars.
708 In general, the evaluation of OMEGA (0.35 to 5.2 μm) and CRISM (0.362 to 3.92 μm)
709 measurements in the VNIR-SWIR spectral range (visible/near to shortwave infrared) leading to
710 the assessment of the mineral phases present on the planet's surface and their composition,
711 follows the 'spectral unmixing' approach, requiring reference endmember spectra (Cloutis et al.
712 2006; Combe et al. 2008; Mangold et al. 2008; Bishop et al. 2009; Lichtenberg et al. 2010; Roach
713 et al. 2010; Noel et al. 2015; Liu et al. 2016). In brief, using the reference endmember spectra, the
714 spectral signal from orbiter measurements is fitted by least-squares techniques, after its correction
715 for the instrumental function (CRISM smile, etc.), atmospheric scattering and incidence angle,
716 using detailed knowledge of Mars topography simultaneously verified by MOLA (Mars Orbital

Laser Altimeter). While to date, only pure endmember kieserite and szomolnokite spectra were used for this assessment, the detection of linear trends across the entire kieserite–szomolnokite solid solution presented in this work allows us to derive reference spectra for kieserite–szomolnokite solid solution minerals of intermediate composition and, in theory, to then obtain additional information on the chemistry (i.e., Mg/Fe ratio) of the unknown $(Mg,Fe)SO_4 \cdot H_2O$ kieserite-group mineral at hand, with semi-quantitative results.

However, additional sources of error arise from the use of different correction datasets preceding the actual spectral unmixing procedure. Different versions of the atmospheric correction model used in the evaluation of CRISM spectra may lead to significant changes in the form of the resulting spectrum, even causing errors in the discrimination between kieserite and szomolnokite endmembers in the same region of interest. Such a case can be seen comparing the work of Bishop et al. (2009) to that of Noel et al. (2015), when the latter authors dismissed the presence of Fe-rich kieserite or endmember szomolnokite in Juventae Chasma using a newer parameter set. We nevertheless believe, that at least a semi-quantitative impression as to the Mg/Fe ratio in kieserite-group minerals in a studied region can be obtained from IR spectra, as long as comparable correction routines are used.

As already outlined above, the knowledge of surface temperatures (at least approximate values) during remote measurements facilitates quantitative comparisons, but otherwise ~~only~~ useful semi-quantitative information (better than x_{Fe} ±0.25) may be extracted, especially when combining several spectral features. The attempt to use sulfate-related bands for such considerations is hampered by their wavenumber position being largely insensitive to temperature changes in IR spectra (Fig. 12). Given the limited resolution of orbiter spectra up to date, this will likely prevent any exact observation of the subtle band position changes due to enhanced noise.

A much more promising situation is to be expected considering the higher resolution and low FWHM of Raman bands, which aids in ascertaining their position changes from kieserite to szomolnokite with higher precision. The superior spectral resolution even allows efficient use of the sulfate-related bands, such as the prominent $\nu_{1(SO_4)}$ band (Fig. 14), to infer the Mg/Fe content, with the benefit of their nearly perfect insensitivity to temperature changes. Despite the lack of surface Raman data at the moment, forthcoming rover missions (in particular ExoMars 2020 and Mars 2020) include Raman on-board instruments. Besides, Mars rovers are and will be equipped with thermometers, providing the precise temperature during measurement.

This work considers the behavior of kieserite and szomolnokite, as we know it from Earth, i.e., crystallizing in the above described *C*2/*c* structure type. However, a second 'polymorph' of $MgSO_4 \cdot H_2O$ has been postulated in literature to be present as a stable phase instead of or along with 'classic' kieserite on Mars. This phase has been obtained during dehydration-rehydration studies at Mars-relevant conditions by Wang et al. (2009, 2011) and is often labeled LH-kieserite (LH for 'low humidity'); Jamieson et al. (2014) obtained this 'polymorph' by dehydrating kieserite at 250 °C for one week. The resulting phase shows minor spectral differences compared to 'classic' kieserite, with a slightly different position of the H_2O combination modes in the 4900 cm^{-1} (2.04 μm) region. We are currently working on a paper elucidating the actual character and spectroscopic properties of this second kieserite 'polymorph' in detail.

Crystal field spectra. The main purpose of presenting an optical crystal field (CF) spectrum of szomolnokite in the present context is to provide an impression on the possible influence of the spin-allowed $^5T_{2g}(D) \rightarrow {}^5E_g(D)$ crystal field transition of octahedral Fe^{2+} on remote or in-situ NIR spectra from orbiter and rover missions. Figure 15 shows that the cubic $^5E_g(D)$ state splits into two levels in the low-symmetry field of szomolnokite and that the lower

765 energy $^5A_{1g}$ split level (tetragonal label) centered at 7650 cm^{-1} (1.31 μm) may influence
766 overtones and combinations modes in the NIR spectra from ~5350 cm^{-1} (1.87 μm) onwards. In
767 particular, the first overtone of the H_2O stretching mode is located at 6565 cm^{-1} within the low-
768 energy wing of $^5A_{1g}$, also perceivable in the VNIR DRIFT spectra of szomolnokite acquired by
769 Pitman et al. (2014). Concerning CF states, up to now only the higher-energetic and more intense
770 $^5B_{1g}$ split level at 10640 cm^{-1} (0.94 μm) was attributed to szomolnokite (at 0.9–0.95 μm) and
771 discussed (Cloutis et al. 2006; Bishop et al. 2009; Jamieson et al. 2014; Pitman et al. 2014). It
772 was argued that the latter Fe-related absorption (~0.95 μm) is commonly observed in spectra of
773 Martian sulfate salts and thus may not uniquely identify szomolnokite, since it could also be
774 produced by even minor amounts of particles of a separate Fe-bearing dust phase covering sulfate
775 rocks (Bishop et al. 2009). However, the $^5A_{1g}$ split level at 7640 cm^{-1} (1.31 μm) was not
776 considered so far as diagnostic for szomolnokite, in spite of the fact that it is present, albeit weak,
777 also in the comparative laboratory spectra of szomolnokite by Bishop et al. (2009). Furthermore,
778 in the usual wavelength presentation, this band is broadened compared to the stronger $^5B_{1g}$ band
779 and thus even less noticeable. Admittedly, in Fe-bearing monohydrated sulfate, i.e., in diluted
780 szomolnokite, the electronic $^5A_{1g}$ band will be most likely too weak to be extracted from orbiter
781 spectra, but we propose to regard it as highly diagnostic for szomolnokite in data of future rover
782 missions. Moreover, since the energies of the $^5E_g(D)$ split levels at 7650 and 10640 cm^{-1} are very
783 closely reproduced by the CF calculations at 7713 and 10549 cm^{-1}, respectively (full triclinic SM
784 calculation, Table 10), the influence of temperature as well as of the Mg/Fe ratio in solid
785 solutions can be efficiently predicted from our presented single crystal structure data: for
786 example, a temperature reduction to –160 °C hardly changes the calculated energy of $^5B_{1g}$ (10539
787 cm^{-1}) but predicts a moderate shift of $^5A_{1g}$ by ~100 cm^{-1} to 7815 cm^{-1}; contrary, stronger band

788 shifts are predicted with changing Mg/Fe ratio: for the structure with $Mg_{0.55}Fe_{0.45}$ (Tables 2,3,6)
789 respective energies of 11034 and 8249 cm^{-1} are calculated for ambient conditions.
790
791 **Implications**
792
793 The verification of the existence of a continuous solid solution series between kieserite and
794 szomolnokite suggests that respective intermediate compositions are expected to occur in Fe-rich
795 environments. The presented data can generally assist in the identification of kieserite,
796 szomolnokite and their solid solutions, not only on Mars, despite the attention given to this
797 planet. The linear character of the observed spectral and structural trends at room temperature and
798 the knowledge of their changes upon cooling provides a solid starting basis to draw conclusions
799 about the composition of this important Martian sulfate based on absorption band positions in IR
800 and Raman spectra. Even in the case of a semi-quantitative approach (no knowledge of
801 temperature), zoning of Fe contents in Martian kieserite-containing sediments can be monitored.
802 The presented data are especially relevant in view of the shortly forthcoming rover missions Mars
803 2020 (NASA) and ExoMars 2020 (ESA) allowing in-situ vibrational spectroscopic
804 measurements, including, for the first time on Mars, Raman investigations.
805 Chemical zoning of kieserite-group minerals from past spectral results may also be
806 determined. Promising candidates for such a re-evaluation are, as representative examples, the
807 spatially resolved CRISM spectra acquired across the rather large Ius Chasma and Juventae
808 Chasma sulfate deposits or Aram Chaos.
809
810
811

Acknowledgments

We sincerely thank Melissa D. Lane and an anonymous reviewer for their detailed and thorough comments and opinions, which helped to significantly improve the quality and readability of this paper. Assistance by G. Giester (Vienna) with the low-temperature X-ray data collections is gratefully acknowledged. We also thank R. Miletich, M. Ende, and J. Meusburger (all Vienna) for helpful discussions, and P. Kadlec of the Masaryk University (Brno) for the chemical analyses of our samples. Author MW is grateful to Y.Y. Yeung (Hong Kong) for providing a modified copy of his HCFLDN2 program. This work was supported by a grant from the Austrian Science Fund (FWF): P 29149-N29.

References cited

Arvidson, R.E., Poulet, F., Bibring, J.-P., Wolff, M., Gendrin, A., Morris, R.V., Freeman, J.J., Langevin, Y., Mangold, N., and Belucci, G. (2005) Spectral reflectance and morphologic correlations in eastern Terra Meridiani, Mars. Science, 307, 1591–1594.

Bader, R.F.W. (1998) Atoms in Molecules. In P.v.R. Schleyer, Ed., Encyclopedia of Computational Chemistry vol 1, p. 64-86. John Wiley and Sons, Chichester.

Bechtold, A., and Wildner, M. (2016) Crystal chemistry of the kieserite–cobaltkieserite solid solution, $Mg_{1-x}Co_x(SO_4)\cdot H_2O$: well behaved oddities. European Journal of Mineralogy, 28, 43–52.

Beegle, L.W., Bhartia, R., DeFlores, L., Darrach, M., Kidd, R.D., Abbey, W., Asher, S., Burton, A., Clegg, S., Conrad, P.G., Edgett, K., Ehlmann, B., Langenhorst, F., Fries, M., Hug, W., Nealson, K., Popp, J., Sobron, P., Steele, A., Wiens, R., and Williford, K. (2014) SHERLOC: Scanning Habitable Environments with Raman & Luminescence for Organics & Chemicals, an investigation for 2020. 11th International GeoRaman Conference, 5101.pdf.

Bishop, J.L., Parente, M., Weitz, C.M., Noe Dobrea, E.Z., Roach, L.H., Murchie, S.L., McGuire, P.C., McKeown, N.K., Rossi, C.M., Brown, A.J., Calvin, W.M., Milliken, R., and Mustard, J.F. (2009) Mineralogy of Juventae Chasma: Sulfates in the light-toned mounds, mafic minerals in the bedrock,

and hydrated silica and hydroxylated ferric sulfate on the plateau. Journal of Geophysical Research, 114, E00D09.

Bosi, F., Belardi, G., and Ballirano, P. (2009) Structural features in Tutton's salts $K_2[M^{2+}(H_2O)_6](SO_4)_2$, with M^{2+} = Mg, Fe, Co, Ni, Cu, and Zn. American Mineralogist, 94, 74–82.

Brese, N.E., and O'Keeffe, M. (1991) Bond-valence parameters for solids. Acta Crystallographica, B47, 192–197.

Brown, I.D., and Shannon, R.D. (1973) Empirical bond–strength–bond–length curves for oxides. Acta Crystallographica, A29, 266–282.

Chang, Y.M., Rudowicz, C., and Yeung, Y.Y. (1994) Crystal field analysis of the $3d^N$ ions at low symmetry sites including the "imaginary" terms. Computers in Physics, 8, 583–588.

Chio, C.H., Sharma, S.K., and Muenow, D.W. (2007) The hydrates and deuterates of ferrous sulfate ($FeSO_4$): a Raman spectroscopic study. Journal of Raman Spectroscopy, 38, 87–99.

Christensen, P.R., Bandfield, J.L., Clark, R.N., Edgett, K.S., Hamilton, V.E., Hoefen, T., Kieffer, H.H., Kuzmin, R.O., Lane, M.D., Malin, M.C., Morris, R.V., Pearl, J.C., Pearson, R., Roush, T.L., Ruff, S.W., and Smith, M.D. (2000) Detection of crystalline hematite mineralization on Mars by the Thermal Emission Spectrometer: Evidence for near-surface water. Journal of Geophysical Research, 105, 9623–9642.

Christensen, P.R., Wyatt, M.B., Glotch, T.D., Rogers, A.D., Anwar, S., Arvidson, R.E., Bandfield, J.L., Blaney, D.L., Budney, C., Calvin, W.M., Fallacaro, A., Fergason, R.L., Gorelick, N., Graff, T.G., Hamilton, V.E., Hayes, A.G., Johnson, J.R., Knudson, A.T., McSween, H.Y. Jr., Mehall, G.L., Mehall, L.K., Moersch, J.E., Morris, R.V., Smith, M.D., Squyres, S.W., Ruff, S.W. and Wolff, M.J. (2004) Mineralogy at Meridiani Planum from the Mini-TES experiment on the Opportunity rover. Science, 306, 1733–1739.

Clark, B.C., and Van Hart, D.C. (1981) The salts of Mars. Icarus, 45, 370–378.

Clark, B.C., Morris, R.V., McLennan, S.M., Gellert, R., Jolliff, B., Knoll, A.H., Squyres, S.W., Lowenstein, T.K., Ming, D.W., Tosca, N.J., Yen, A., Christensen, P.R., Gorevan, S., Brückner, J., Calvin, W., Dreibus, G., Farrand, W., Klingelhoefer, G., Waenke, H., Zipfel, J., Bell, J.F. III,

Grotzinger, J., McSween, H.Y., and Rieder, R. (2005) Chemistry and mineralogy of outcrops at Meridiani Planum. Earth and Planetary Science Letters, 240, 73–94.

Cloutis, E.A., Craig, M.A., Mustard, J.F., Kruzelecky, R.V., Jamroz, W.R., Scott, A., Bish, D.L., Poulet, F., Bibring, J.-P., and King, P.L. (2007) Stability of hydrated minerals on Mars. Geophysical Research Letters, 34, L20202.

Combe, J.-Ph., Le Mouélic, S., Sotin, C., Gendrin, A., Mustard, J.F., Le Deit, L., Launeau, P., Bibring, J.-P., Gondet, B., Langevin, Y., and Pinet, P. (2008) Analysis of OMEGA/Mars Express hyperspectral data using a Multiple-Endmember Linear Spectral Unmixing Model (MELSUM): Methodology and first results. Planetary and Space Science, 56, 951–975.

Dobrolenskiy, Y.S., Korablev, O.I., Fedorova, A.A., Mantsevich, S.N., Kalinnikov, Y.K., Vyazovetskiy, N.A., Titov, A.Y., Stepanov, A.V., Sapgir, A.G., Alexandrov, K.V., Evdokimova, N.A., and Kuzmin, R.O. (2017) European Planetary Science Congress Abstracts, 11, 255.

Downs, R.T., Gibbs, G.V., Bartelmehs, K.L., and Boisen, M.B. Jr. (1992) Variations of bond lengths and volumes of silicate tetrahedra with temperature. American Mineralogist, 77, 751–757.

Dyar, M.D., and Schaefer, M.W. (2004) Mössbauer spectroscopy on the surface of Mars: constraints and expectations. Earth and Planetary Science Letters, 218, 243–259.

Dyar, M.D., Breves, E., Jawin, E., Marchand, G., Nelms, M., O'Connor, V., Peel, S., Rothstein, Y., Sklute, E.C., Lane, M.D., Bishop, J.L., and Mertzman, S.A. (2013) Mössbauer parameters of iron in sulfate minerals. American Mineralogist, 98, 1943–1965.

Feldman, W.C., Mellon, M.T., Maurice, S., Prettyman, T.H., Carey, J.W., Vaniman, D.T., Bish, D.L., Fialips, C.I., Chipera, S.J., Kargel, J.S., Elphic, R.C., Funsten, H.O., Lawrence, D.J., and Tokar, R.L. (2004) Hydrated states of $MgSO_4$ at equatorial latitudes on Mars. Geophysical Research Letters, 31, L16702.

Figgis, B.N., and Hitchman, M.A. (2000) Ligand field theory and its applications, 364p. Wiley-VCH, New York.

Gagné, O., Hawthorne, F.C., Shannon, R.D., and Fischer, R.X. (2018) Empirical electronic polarizabilities: deviations from the additivity rule. I. $M^{2+}SO_4 \cdot nH_2O$, blödite $Na_2M^{2+}(SO_4)_2 \cdot 4H_2O$, and

892 kieserite-related minerals with sterically strained structures. Physics and Chemistry of Minerals, 45,
893 303–310.
894 Gendrin, A., Mangold, N., Bibring, J.-P., Langevin, Y., Gondet, B., Poulet, F., Bonello, G., Quantin, C.,
895 Mustard, J., Arvidson, R., and LeMouélic, S. (2005) Sulfates in Martian layered terrains: the
896 OMEGA/Mars Express view. Science, 307, 1587–1591.
897 Giester, G. (1988) The crystal structures of $CuSO_4 \cdot H_2O$ and $CuSeO_4 \cdot H_2O$, and their relationships to
898 kieserite. Mineralogy and Petrology, 38, 277–284.
899 Giester, G., and Wildner, M. (1992) The crystal structures of kieserite-type compounds. II. Crystal
900 structures of $Me(II)SeO_4 \cdot H_2O$ (Me = Mg,Mn,Co,Ni,Zn). Neues Jahrbuch Mineralogischer
901 Monatshefte, 1992, 135–144.
902 Glotch, T.D., Bandfield, J.L., Christensen, P.R., Calvin, W.M., McLennan, S., Clark, B.C., Rogers, A.D.,
903 and Squyres, S.W. (2006) Mineralogy of the light-toned outcrop at Meridiani Planum as seen by the
904 Miniature Thermal Emission Spectrometer and implications for its formation. Journal of Geophysical
905 Research, 111, E12S03.
906 Griffen, D.T., and Ribbe, P.H. (1979) Distortions in the tetrahedral oxyanions of crystalline substances.
907 Neues Jahrbuch Mineralogischer Abhandlungen, 137, 54–73.
908 Hawthorne, F.C., Groat, L.A., Raudsepp, M., and Ercit, T.S. (1987) Kieserite, $Mg(SO_4)(H_2O)$, a titanite-
909 group mineral. Neues Jahrbuch Mineralogischer Abhandlungen, 157, 121–132.
910 Jamieson, C.S., Noe Dobrea, E.Z., Dalton, J.B. III, Pitman, K.M., and Abbey, W.Z. (2014) The spectral
911 variability of kieserite ($MgSO_4 \cdot H_2O$) with temperature and grain size and its application to the Martian
912 surface. Journal of Geophysical Research: Planets, 119, 1218–1237.
913 Karunatillake, S., Wray, J.J., Gasnault, O., McLennan, S.M., Rogers, A.D., Squyres, S.W., Boynton,
914 W.V., Skok, J.R., Ojha, L., and Olsen, N. (2014) Sulfates hydrating bulk soil in the Martian low and
915 middle latitudes. Geophysical Research Letters, 41, 7987–7996.
916 Keil, K., Clark, B.C., Baird, A.K., Toulmin, P. III, and Rose, H.J.J. (1978) Zur Chemie der
917 Marsoberfläche. Mineralogische und petrologische Implikationen. Naturwissenschaften, 65, 231–238.

Knauth, L.P., Burt, D.M., and Wohletz, K.H. (2005) Impact origin of sediments at the Opportunity landing site on Mars. Nature, 438, 1123–1128.

Lane, M.D. (2007) Mid-infrared emission spectroscopy of sulfate and sulfate-bearing minerals. American Mineralogist, 92, 1–18.

Lane, M.D., Bishop, J.L., Dyar, M.D., Hiroi, T., Mertzman, S.A., Bish, D.L., King, P.L., and Rogers, A.D. (2015) Mid-infrared emission spectroscopy and visible/near-infrared reflectance spectroscopy of Fe-sulfate minerals. American Mineralogist, 100, 66–82.

Libowitzky, E. (1999) Correlation of O–H stretching frequencies and O–H···O hydrogen bond lengths in minerals. Monatshefte für Chemie, 130, 1047–1059.

Lichtenberg, K.A., Arvidson, R.E., Morris, R.V., Murchie, S.L., Bishop, J.L., Fernández-Remolar, D., Glotch, T.D., Dobrea, E.N., Mustard, J.F., Andrews-Hanna, J., and Roach, L.H. (2010) Stratigraphy of hydrated sulfates in the sedimentary deposits of Aram Chaos, Mars. Journal of Geophysical Research, 115, E00D17.

Liu, Y., Glotch, T.D., Scudder, N.A., Kraner, M.L., Condus, T., Arvidson, R.E., Guinness, E.A., Wolff, M.J., and Smith, M.D. (2016) End-member identification and spectral mixture analysis of CRISM hyperspectral data: A case study on southwest Melas Chasma, Mars. Journal of Geophysical Research: Planets, 121, 2004–2036.

Mangold, N., Gendrin, A., Gondet, B., LeMouelic, S., Quantin, C., Ansan, V., Bibring, J.-P., Langevine, Y., Masson, P., and Nukum, G. (2008) Spectral and geologic study of the sulfate-rich region of West Candor Chasma, Mars. Icarus, 194, 519–543.

Milliken, R.E., Mustard, J.F., Poulet, F., Jouglet, D., Bibring, J.-P., Gondet, B., and Langevin, Y. (2007) Hydration state of the Martian surface as seen by Mars Express OMEGA: 2. H_2O content of the surface. Journal of Geophysical Research, 112, E08S07.

Morrison, S.M., Downs, R.T., Blake, D.F., Prabhu, A., Eleish, A., Vaniman, D.T., Ming, D.W., Rampe, E.B., Hazen, R.M., Achilles, C.N., Treiman, A.H., Yen, A.S., Morris, R.V., Bristow, T.F., Chipera, S.J., Sarrazin, P.C., Fendrich, K.V., Morookian, J.M., Farmer, J.D., Des Marais, D.J., and Craig, P.I.

(2018) Relationships between unit-cell parameters and composition for rock-forming minerals on Earth, Mars, and other extraterrestrial bodies. American Mineralogist, 103, 848–856.

Noel, A., Bishop, J.L., Al-Samir, M., Gross, C., Flahaut, J., McGuire, P.C., Weitz, C.M., Seelos, F., and Murchie, S. (2015) Mineralogy, morphology and stratigraphy of the light-toned interior layered deposits at Juventae Chasma. Icarus, 251, 315–331.

Nonius (1998) Kappa CCD program package. Nonius B.V., Delft.

Papike, J.J., Burger, P.V., Karner, J.M., and Shearer, C.K. (2007) Mars surface mineralogy: Implications of kieserite group crystal chemistry $(Mg,Fe^{2+},Mn^{2+},Zn,Ni,Co)SO_4 \cdot H_2O$. 7th International Conference on Mars, 3004.pdf.

Pitman, K.M., Noe Dobrea, E.Z., Jamieson, C.S., Dalton, J.B. III, Abbey, W.J., and Joseph, E.C.S. (2014) Reflectance spectroscopy and optical functions for hydrated Fe-sulfates. American Mineralogist, 99, 1593–1603.

Powell, R., and Holland, T. (1993) On the formulation of simple mixing models for complex phases. American Mineralogist, 78, 1174–1180.

Roach, L.H., Mustard, J.F., Swayze, G., Milliken, R.E., Bishop, J.L., Murchie, S.L., and Lichtenberg, K. (2010) Hydrated mineral stratigraphy of Ius Chasma, Valles Marineris. Icarus, 206, 253–268.

Robinson, K., Gibbs, G.V., and Ribbe, P.H. (1971) Quadratic elongation: a quantitative measure of distortion in coordination polyhedra. Science, 172, 567–570.

Rull, F. (2018) Mars mineralogy: The EXOMARS 2020 approach. Acta Crystallographica, A74, e55.

Rull, F., Maurice, S., Hutchinson, I., Moral, A., Perez, C., Diaz, C., Colombo, M., Belenguer, T., Lopez-Reyes, G., Sansano, A., Forni, O., Parot, Y., Striebig, N.,Woodward, S., Howe, C., Tarcea, N., Rodriguez, P., Seoane, L., Santiago, A., Rodriguez-Prieto, J.A., Medina, J., Gallego, P., Canchal, R., Santamaría, P., Ramos, G., and Vago, J.L. (2017) The Raman laser spectrometer for the ExoMars rover mission to Mars. Astrobiology, 17, 627–654.

Schröder, C., Klingelhöfer, G., and Tremel, W. (2004) Weathering of Fe-bearing minerals under Martian conditions, investigated by Mössbauer spectroscopy. Planetary and Space Science, 52, 997–1010.

970 Shannon, R.D. (1976) Revised effective ionic radii and systematic studies of interatomic distances in
971 halides and chalcogenides. Acta Crystallographica, A32, 751–767.
972 Sheldrick, G.M. (2008) A short history of SHELX. Acta Crystallographica, A64, 112–122.
973 Stoilova, D., and Lutz, H.D. (1998) Infrared study of ν_{OD} modes in isotopically dilute (HDO) kieserite-
974 type compounds $MXO_4 \cdot H_2O$ (M = Mn, Co, Ni, Zn, and X = S, Se) with matrix-isolated M'^{2+} and
975 $X'O_4^{2-}$ guest ions. Journal of Molecular Structure, 450, 101–106.
976 Stoilova, D., and Wildner, M. (2004) Blödite-type compounds $Na_2Me^{2+}(SO_4)_2 \cdot 4H_2O$ (Me = Mg, Co, Ni,
977 Zn): crystal structures and hydrogen bonding systems. Journal of Molecular Structure, 706, 57–63.
978 van Hinsberg,V.J., Vriend, S.P., and Schumacher, J.C. (2005a) A new method to calculate end-member
979 thermodynamic properties of minerals from their constituent polyhedra I: enthalpy, entropy and molar
980 volume. Journal of Metamorphic Geology, 23, 165–179.
981 van Hinsberg,V.J., Vriend, S.P. , and Schumacher, J.C. (2005b) A new method to calculate end-member
982 thermodynamic properties of minerals from their constituent polyhedra II: heat capacity,
983 compressibility and thermal expansion. Journal of Metamorphic Geology, 23, 681–693.
984 Wang, A., Freeman, J.J., and Jolliff, B.L. (2009) Phase transition pathways of the hydrates of magnesium
985 sulfate in the temperature range 50°C to 5°C: Implication for sulfates on Mars. Journal of Geophysical
986 Research, 114, E04010.
987 Wang, A., Freeman, J.J., Chou, I.-M., and Jolliff, B.L. (2011) Stability of Mg-sulfates at –10°C and the
988 rates of dehydration/rehydration processes under conditions relevant to Mars. Journal of Geophysical
989 Research, 116, E12006.
990 Wiens, R.C., Maurice, S., and Rull Perez, F.P. (2017a) The SuperCam remote sensing instrument suite for
991 the Mars 2020 rover: A preview. Spectroscopy, 32, 50–55.
992 Wiens, R.C., Newell, R., Clegg, S., Sharma, S.K., Misra, A., Bernardi, P., Maurice, S., McCabe, K., Cais,
993 P., and the SuperCam Science Team (2017b) The SuperCam remote Raman spectrometer for Mars
994 2020. Lunar and Planetary Science XLVIII, 2600.pdf.
995 Wildner, M. (1992) On the geometry of $Co(II)O_6$ polyhedra in inorganic compounds. Zeitschrift für
996 Kristallographie, 202, 51–70.

997 Wildner, M. (1996) Polarized electronic absorption spectra of Co^{2+} ions in the kieserite-type compounds
998 $CoSO_4 \cdot H_2O$ and $CoSeO_4 \cdot H_2O$. Physics and Chemistry of Minerals, 23, 489–496.
999 Wildner, M., and Giester, G. (1991) The crystal structures of kieserite-type compounds. I. Crystal
1000 structures of Me(II)$SO_4 \cdot H_2O$ (Me = Mn,Fe,Co,Ni,Zn). Neues Jahrbuch Mineralogischer Monatshefte,
1001 1991, 296–306.
1002 Wildner, M., Beran, A., and Koller, F. (2013) Spectroscopic characterisation and crystal field calculations
1003 of varicoloured kyanites from Loliondo, Tanzania. Mineralogy and Petrology, 107, 289–310.
1004 Witzke, A., Arnold, G., and Stöffler, D. (2007) Spectral detectability of Ca- and Mg-sulphates in Martian
1005 bright soils in the 4-5 μm wavelength range. Planetary and Space Science, 55, 429–440.
1006
1007
1008 **Figure captions**
1009
1010 **Figure 1.** Deviations between actual Fe content of the $Mg_{1-x}Fe_x(SO_4) \cdot H_2O$ solid solution samples
1011 $x_{Fe(sample)}$ as determined by the wet chemical analyses and the pre-adjusted Mg/Fe ratio in the
1012 hydrothermal batch $x_{Fe(preset)}$. Errors are equal or smaller than the symbol size. Note that batches
1013 exceeding the shown range of deviation (i.e., mainly Mg-dominant batch runs with metallic Fe-
1014 foil as redox buffer yielding significantly Fe-enriched samples) were not used for the
1015 spectroscopic measurements.
1016
1017 **Figure 2.** Variation of the lattice parameters (**a**) a, b, c and (**b**) β and V along the
1018 $Mg_{1-x}Fe_x(SO_4) \cdot H_2O$ solid solution series with linear regression lines. Errors are equal or smaller
1019 than the symbol size. The data for endmember kieserite are taken from Bechtold and Wildner
1020 (2016). Previous data for the Fe endmember (Wildner and Giester 1991) are shown (without
1021 errors) as dotted diamond symbols.

Figure 3. Polyhedral geometries along the $Mg_{1-x}Fe_x(SO_4)\cdot H_2O$ solid solution series with linear regression lines, (**a**) octahedral Me–O bond lengths and (**b**) O–Me–O angles, (**c**) tetrahedral S–O bond lengths and (**d**) O–S–O angles. If not indicated, errors are equal or smaller than the symbol size. The data for endmember kieserite are taken from Bechtold and Wildner (2016). Previous data for the Fe endmember (Wildner and Giester 1991) are shown (without errors) as dotted diamond symbols.

Figure 4. (**a**) Polyhedral volumes, (**b**) Me–O–S and Me–O–Me angles and (**c**) hydrogen bond lengths along the $Mg_{1-x}Fe_x(SO_4)\cdot H_2O$ solid solution series with linear regression lines. For (**a**), note the strongly different scales for the tetrahedral and octahedral volumes. If not indicated, errors are equal or smaller than the symbol size. The data for endmember kieserite are taken from Bechtold and Wildner (2016). Previous data for the Fe endmember (Wildner and Giester 1991) are shown (without errors) as dotted diamond symbols.

Figure 5. Overlay of crystal structure fragments of kieserite, $MgSO_4\cdot H_2O$ (full lines), in front of szomolnokite, $FeSO_4\cdot H_2O$ (dashed lines), centred at the S atom (0,*y*,¼), in a projection along the negative *b*-axis. MgO_6 octahedra are shown in grey, FeO_6 octahedra below in green, SO_4 tetrahedra in yellow, and the water molecules as cyan spheres. Dotted arrows indicate major rotational and translational changes along the $Mg_{1-x}Fe_x(SO_4)\cdot H_2O$ solid solution series as discussed in the text. Cell axes plots are scaled to 50%. Structural data for endmember kieserite are taken from Bechtold and Wildner (2016).

Figure 6. Variation of the lattice parameters (**a**) *a*, *b*, *c* and (**b**) β and *V* for kieserite ('Mg', light grey circle symbols) and szomolnokite ('Fe', dark grey diamond symbols) within the investigated

1047 temperature range, with second-order regression lines. Errors are equal or smaller than the
1048 symbol size.
1049
1050 **Figure 7.** Variation of the polyhedral geometries (**a**) octahedral Me–O bond lengths and (**b**) O–
1051 Me–O angles, (**c**) polyhedral volumes, and (**d**) tetrahedral S–O bond lengths (uncorrected for
1052 thermal motion, see text) for kieserite ('Mg', light grey circle symbols) and szomolnokite ('Fe',
1053 dark grey diamond symbols) within the investigated temperature range, with second- or third
1054 order regression lines. Third-order regressions are very probably not significant, but are used to
1055 guide the eye. For (**c**), note the somewhat different scales for the tetrahedral and octahedral
1056 volumes. If not indicated, errors are equal or smaller than the symbol size.
1057
1058 **Figure 8.** Variation of (**a**) hydrogen bond lengths and (**b**) Me–O–S/Me angles for kieserite ('Mg',
1059 light grey circle symbols) and szomolnokite ('Fe', dark grey diamond symbols) within the
1060 investigated temperature range, with second-order regression lines. If not indicated, errors are
1061 equal or smaller than the symbol size.
1062
1063 **Figure 9.** FTIR spectra of the kieserite and szomolnokite endmembers, $Mg/Fe(SO_4)\cdot H_2O$, in each
1064 measuring mode. In addition to band position changes between the endmembers, note the
1065 differences in band positions and shapes between the measuring modes.
1066
1067 **Figure 10.** Spectral region with three diagnostic H_2O combination modes, (**a**) observed in DRIFT
1068 measurements on undiluted sample material, (**b**) detailed plot of band position change for the
1069 examined bands across the kieserite–szomolnokite solid solution series. Errors equal or smaller
1070 than the symbol size are not plotted.
1071

Figure 11. Dependence of the positions of relevant FTIR absorption features (transmission measurements) of $Mg_{1-x}Fe_x(SO_4)\cdot H_2O$ solid solutions on the Fe content at room temperature (RT). The scatter in data points of the $\nu_{3(H_2O)}$ vibration is caused by the significant overlap with the $\nu_{1(H_2O)}$ vibration. Errors equal or smaller than the symbol size are not plotted.

Figure 12. Dependence of the FTIR absorption band positions of $Mg_{1-x}Fe_x(SO_4)\cdot H_2O$ solid solutions on temperature, as seen in transmission mode. The two most promising candidate bands for the determination of x_{Fe} based on FTIR spectra are shown by rectangular symbols.

Figure 13. Dependence of the Raman band positions of $Mg_{1-x}Fe_x(SO_4)\cdot H_2O$ solid solutions on increasing Fe content x_{Fe} at room temperature. Errors are equal or smaller than the symbol size.

Figure 14. Raman spectra of the kieserite and szomolnokite endmembers, $Mg/Fe(SO_4)\cdot H_2O$, at room temperature.

Figure 15. UV-Vis-NIR absorption spectrum of szomolnokite in the range from 28800–3500 cm^{-1} with observed (bold line marks) and calculated energy levels (thin line marks) and respective assignments for cubic symmetry, in case of spin-allowed $^5E_g(D)$ also with tetragonal labels. Calculated singlet states are not shown. The inset shows the background-subtracted and intensity-enhanced region between 27000–18000 cm^{-1}.

1098 **Tables**

1099

1100 **Table 1.** Composition of the spectroscopically studied samples as determined by wet chemical
1101 analyses. The analytical error is 0.005 wt% for Mg and 0.002 wt% for Fe. Deviations of the
1102 actual sample Fe content $x_{Fe(sample)}$ from the preset Mg/Fe ratio in the batch $x_{Fe(preset)}$ are also
1103 given. The Mg/Fe ratios of individual hand-picked crystals for single crystal X-ray diffraction
1104 studies were extracted as variable parameter in the respective structure refinement runs.

1105

Sample ID	Mg (wt%)	Fe (wt%)	$x_{Fe(sample)}$	$x_{Fe(preset)}$	$x_{Fe(sample)} - x_{Fe(preset)}$
Fe10c	15.77	3.73	0.093	0.100	-0.006
Fe15c	13.84	6.54	0.170	0.150	0.020
Fe20c	13.05	7.53	0.200	0.200	0.000
Fe30c	11.87	9.68	0.261	0.300	-0.038
Fe40c	9.85	12.78	0.360	0.400	-0.039
Fe5Sa	15.81	3.89	0.096	0.050	0.046
Fe10Sa	14.21	5.42	0.142	0.100	0.042
Fe15Sa	12.77	7.63	0.206	0.150	0.056
Fe25Sa	11.05	10.25	0.287	0.250	0.037
Fe45Sa	7.68	15.84	0.473	0.450	0.023
Fe65Sa	4.67	20.78	0.659	0.650	0.009
Fe85Sa	2.36	23.04	0.868	0.850	0.018
Fe0Sb	16.76	0.05	0.000	0.000	0.000
Fe20Sa	11.87	8.81	0.244	0.200	0.044
Fe30Sa	9.85	12.22	0.350	0.300	0.050
Fe35Sa	8.82	14.17	0.411	0.350	0.061
Fe40Sa	8.10	14.36	0.435	0.400	0.035
Fe50Sa	6.41	17.99	0.549	0.500	0.049
Fe60Sa	5.14	19.87	0.627	0.600	0.027
Fe70Sa	3.85	22.03	0.713	0.700	0.013
Fe75Sa	3.28	22.65	0.750	0.750	0.000
Fe80Sa	2.36	23.04	0.809	0.800	0.009
Fe90Sa	0.92	24.71	0.920	0.900	0.020
Fe95Sa	0.69	27.19	0.945	0.950	-0.004
Fe100Sa	0.01	27.5	0.999	1.000	0.000
Fe5Sc	15.89	3.64	0.090	0.050	0.040
Fe80Sc	3.34	22.93	0.749	0.800	-0.050
Fe85Sc	2.49	23.96	0.807	0.850	-0.042
Fe0Sc	17.59	0	0	0	0

Table 2. Crystal data and details of room-temperature X-ray data collections and structure refinements for selected representatives of the $Mg_{1-x}Fe_x(SO_4)\cdot H_2O$ solid solution series. Common data: monoclinic, space group $C2/c$ (no. 15), $Z = 4$. Data for the kieserite endmember are taken from Bechtold and Wildner (2016).

$Mg_{1-x}Fe_x(SO_4)\cdot H_2O$	$Mg_{1.00}Fe_{0.00}$	$Mg_{0.86}Fe_{0.14}$	$Mg_{0.55}Fe_{0.45}$	$Mg_{0.25}Fe_{0.75}$	$Mg_{0.00}Fe_{1.00}$
x_{Fe}	0.0	0.138(2)	0.450(2)	0.752(3)	1.0
a (Å)	6.910(1)	6.938(1)	6.989(1)	7.042(1)	7.086(1)
b (Å)	7.634(2)	7.621(1)	7.601(1)	7.579(2)	7.555(1)
c (Å)	7.643(2)	7.663(1)	7.710(1)	7.753(2)	7.780(1)
β (°)	118.00(1)	118.14(1)	118.30(1)	118.49(1)	118.61(1)
V (Å^3)	356.00(14)	357.32(8)	360.63(8)	363.65(14)	365.63(8)
μ (mm^{-1})	0.97	1.48	2.61	3.70	4.58
D_{calc} (gcm^{-3})	2.582	2.653	2.810	2.961	3.087
Exposure time (s)/frame	140	150	25	70	40
CCD frames processed	508	526	503	514	511
Frame scale factors $_{max, min}$	1.11, 0.89	1.12, 0.91	1.16, 0.81	1.17, 0.76	1.09, 0.77
Total number of intensity data	12919	14115	13849	14055	12661
Total number of reflections	8865	8935	8613	8615	8875
Intensity data for unit cell	5101	7219	7420	7418	5362
Number of hkl's	3995	4178	4203	4211	4255
Unique hkl's	1089	1100	1110	1126	1133
R_i (%)	3.20	2.77	2.37	3.09	2.65
$F_o > 4\sigma(F_o)$	937	985	1026	1027	1111
Variables	39	42	42	42	40
wR2 [for all F_o^2] (%)	6.17	5.75	5.72	5.98	4.12
weighting parameters a, b[a]	0.028, 0.20	0.027, 0.27	0.028, 0.20	0.030, 0.32	0.018, 0.27
R1 [for $F_o > 4\sigma(F_o)$] (%)	2.27	2.23	2.20	2.39	1.56
R1 [for all F_o] (%)	2.94	2.73	2.53	2.82	1.60
Goodness of fit	1.109	1.062	1.151	1.073	1.065
Extinction coefficient	0	0.004(2)	0.009(2)	0.009(2)	0.260(5)
$\Delta\rho_{max, min}$ (e$^-$ Å^{-3})	0.47, -0.51	0.59, -0.43	0.95, -0.45	1.02, -0.49	0.77, -0.62

[a] $w = 1 / [\sigma^2(F_o^2) + (a\times P)^2 + b\times P]$; $P = \{[\max of (0 or F_o^2)] + 2F_c^2\} / 3$.

This is a preprint, the final version is subject to change, of the American Mineralogist (MSA)
Cite as Authors (Year) Title. American Mineralogist, in press.
DOI: https://doi.org/10.2138/am-2019-6983

Table 3. Structure parameters at room temperature for selected representatives of the $Mg_{1-x}Fe_x(SO_4)\cdot H_2O$ solid solution series. U_{ij} are given in pm^2. Wyckoff positions: Mg/Fe on 4*b* (sym $\bar{1}$): 0,½,0 etc.; S and O3 on 4*e* (sym 2): 0,*y*,¼ etc., $U_{23}=U_{12}=0$; O1, O2 and H on 8*f* (sym 1): *x*,*y*,*z* etc. Respective data for endmember kieserite are given in Bechtold and Wildner (2016).

$Mg_{1-x}Fe_x(SO_4)\cdot H_2O$		$Mg_{0.86}Fe_{0.14}$	$Mg_{0.55}Fe_{0.45}$	$Mg_{0.25}Fe_{0.75}$	$Mg_{0.00}Fe_{1.00}$
Mg/Fe	x_{Fe}	0.138(2)	0.450(2)	0.752(3)	1.0
	U_{11}	81(1)	86(1)	90(1)	81(1)
	U_{22}	93(2)	97(1)	101(1)	93(1)
	U_{33}	88(1)	100(1)	99(1)	91(1)
	U_{23}	6(1)	7(1)	8(1)	9(1)
	U_{13}	35(1)	39(1)	41(1)	38(1)
	U_{12}	–4(1)	–3(1)	–2(1)	–1(1)
	U_{eq}	90(1)	96(1)	98(1)	90(1)
S	*y*	0.15459(3)	0.15413(3)	0.15362(4)	0.15329(3)
	U_{11}	63(1)	67(1)	70(1)	57(1)
	U_{22}	78(1)	81(1)	84(1)	73(1)
	U_{33}	89(1)	101(1)	100(1)	91(1)
	U_{13}	30(1)	34(1)	36(1)	31(1)
	U_{eq}	79(1)	86(1)	87(1)	75(1)
O1	*x*	0.17509(10)	0.17307(10)	0.17096(12)	0.16934(9)
	y	0.04446(9)	0.04384(9)	0.04312(12)	0.04258(9)
	z	0.39481(10)	0.39605(10)	0.39722(12)	0.39810(9)
	U_{11}	94(2)	105(2)	107(3)	91(2)
	U_{22}	162(3)	174(3)	179(3)	170(2)
	U_{33}	161(3)	178(3)	182(3)	177(2)
	U_{23}	70(2)	74(2)	79(3)	80(2)
	U_{13}	39(2)	47(2)	50(2)	51(2)
	U_{12}	41(2)	46(2)	47(2)	44(2)
	U_{eq}	148(1)	160(1)	164(1)	151(1)
O2	*x*	0.09221(10)	0.09347(10)	0.09476(12)	0.09619(9)
	y	0.26771(8)	0.26779(8)	0.26783(10)	0.26810(7)
	z	0.15040(10)	0.15273(10)	0.15504(12)	0.15713(8)
	U_{11}	135(2)	141(2)	145(3)	128(2)
	U_{22}	119(2)	130(2)	132(3)	122(2)
	U_{33}	173(2)	190(3)	190(3)	177(2)
	U_{23}	53(2)	53(2)	53(2)	53(2)
	U_{13}	95(2)	101(2)	103(2)	94(2)
	U_{12}	14(2)	16(2)	14(2)	15(2)
	U_{eq}	133(1)	144(1)	146(1)	134(1)
O3	*y*	0.63647(12)	0.63940(12)	0.64236(15)	0.64477(10)
	U_{11}	117(3)	122(3)	130(4)	125(3)
	U_{22}	134(3)	139(3)	149(4)	131(3)
	U_{33}	118(3)	133(3)	132(4)	116(3)
	U_{13}	58(3)	63(3)	62(3)	62(2)
	U_{eq}	122(1)	131(1)	137(2)	122(1)
H	*x*	0.097(3)	0.094(3)	0.102(3)	0.099(3)
	y	0.698(2)	0.704(3)	0.710(3)	0.717(3)
	z	0.285(3)	0.287(3)	0.290(3)	0.294(3)
	U_{iso}	323(47)	355(50)	372(60)	354(46)

Table 4. Crystal data and details of selected temperature-dependent X-ray data collections and structure refinements for kieserite and szomolnokite endmembers, $Mg/Fe(SO_4)\cdot H_2O$. Common data: monoclinic, space group $C2/c$ (no. 15), $Z = 4$; Exposure time/frame 20 s; 40 variables. Respective room-temperature data for kieserite (Bechtold and Wildner 2016) and szomolnokite are given in Table 1.

$Mg/Fe(SO_4)\cdot H_2O$	$Mg_{1.00}$	$Mg_{1.00}$	$Fe_{1.00}$	$Fe_{1.00}$
T (°C)	–80	–160	–80	–160
a (Å) [a]	6.882(1)	6.865(1)	7.058(1)	7.040(1)
b (Å) [a]	7.653(1)	7.668(1)	7.566(1)	7.576(1)
c (Å) [a]	7.617(1)	7.606(1)	7.758(1)	7.745(1)
β (°) [a]	117.88(1)	117.79(1)	118.45(1)	118.37(1)
V (Å^3)	354.60(9)	354.18(9)	364.23(9)	363.48(9)
μ (mm^{-1})	0.97	0.97	4.60	4.61
D_{calc} (gcm^{-3})	2.592	2.595	3.099	3.105
CCD frames processed	748	748	766	766
Transmission factors $_{max, min}$	0.69, 0.75	0.69, 0.75	0.57, 0.75	0.58, 0.75
Total number of reflections	10428	10307	10851	10783
Intensity data for unit cell	6649	7061	8498	8607
Unique hkl's	1098	1097	1131	1128
R_i (%)	1.96	1.84	2.60	2.30
$F_o > 4\sigma(F_o)$	1047	1054	1112	1118
wR2 [for all F_o^2] (%)	4.48	4.26	3.38	3.22
weighting parameters a, b [b]	0.020, 0.18	0.018, 0.21	0.015, 0.20	0.013, 0.24
R1 [for $F_o > 4\sigma(F_o)$] (%)	1.56	1.48	1.28	1.27
R1 [for all F_o] (%)	1.67	1.56	1.31	1.29
Goodness of fit	1.202	1.207	1.168	1.193
Extinction coefficient	0.004(2)	0.006(2)	0.033(1)	0.042(1)
$\Delta\rho_{max, min}$ (e^- Å^{-3})	0.49, -0.37	0.46, -0.40	0.49, -0.52	0.68, -0.44

[a] lattice parameters are corrected to comply with data from Nonius Kappa CCD room temperature measurements of the very same two crystals (see Experimental section).

[b] $w = 1 / [\sigma^2(F_o^2) + (a\times P)^2 + b\times P]$; $P = \{[\max of (0 or F_o^2)] + 2F_c^2\} / 3$.

Table 5. Selected temperature-dependent structure parameters for kieserite and szomolnokite, $Mg/Fe(SO_4)\cdot H_2O$. U_{ij} are given in pm^2. Wyckoff positions: Mg/Fe on 4*b* (sym $\bar{1}$): 0,½,0 etc.; S and O3 on 4*e* (sym 2): 0,*y*,¼ etc., $U_{23}=U_{12}=0$; O1, O2 and H on 8*f* (sym 1): *x*,*y*,*z* etc. Respective room-temperature data for kieserite are given in Bechtold and Wildner (2016), those for szomolnokite in Table 2.

$Mg/Fe(SO_4)\cdot H_2O$		$Mg_{1.00}$ (–80 °C)	$Mg_{1.00}$ (–160 °C)	$Fe_{1.00}$ (–80 °C)	$Fe_{1.00}$ (–160 °C)
Mg/Fe	U_{11}	49(1)	39(1)	53(1)	36(1)
	U_{22}	60(1)	45(1)	57(1)	38(1)
	U_{33}	57(1)	43(1)	63(1)	42(1)
	U_{23}	2(1)	1(1)	6(1)	5(1)
	U_{13}	22(1)	17(1)	27(1)	18(1)
	U_{12}	–3(1)	–2(1)	–0(1)	0(1)
	U_{eq}	57(1)	43(1)	58(1)	39(1)
S	*y*	0.15635(2)	0.15710(2)	0.15447(2)	0.15512(2)
	U_{11}	35(1)	27(1)	38(1)	28(1)
	U_{22}	46(1)	34(1)	46(1)	33(1)
	U_{33}	54(1)	38(1)	65(1)	44(1)
	U_{13}	18(1)	13(1)	23(1)	16(1)
	U_{eq}	46(1)	34(1)	51(1)	35(1)
O1	*x*	0.17541(7)	0.17522(7)	0.16874(7)	0.16853(7)
	y	0.04664(6)	0.04770(6)	0.04405(7)	0.04497(6)
	z	0.39602(7)	0.39686(6)	0.39968(7)	0.40047(7)
	U_{11}	58(2)	42(1)	63(2)	46(1)
	U_{22}	102(2)	73(2)	111(2)	77(2)
	U_{33}	102(2)	70(1)	120(2)	79(2)
	U_{23}	44(1)	29(1)	54(1)	35(1)
	U_{13}	28(1)	19(1)	35(1)	23(1)
	U_{12}	27(1)	19(1)	30(1)	21(1)
	U_{eq}	91(1)	65(1)	102(1)	70(1)
O2	*x*	0.09440(7)	0.09574(7)	0.09854(7)	0.09991(7)
	y	0.26900(6)	0.26975(5)	0.26941(6)	0.27015(6)
	z	0.15044(7)	0.15109(6)	0.15838(7)	0.15910(6)
	U_{11}	81(2)	59(2)	83(2)	61(2)
	U_{22}	76(2)	57(1)	80(2)	56(2)
	U_{33}	108(2)	75(1)	122(2)	83(2)
	U_{23}	32(1)	21(1)	34(1)	22(1)
	U_{13}	59(1)	42(1)	63(1)	45(1)
	U_{12}	6(1)	2(1)	7(1)	3(1)
	U_{eq}	82(1)	60(1)	89(1)	62(1)
O3	*y*	0.63431(8)	0.63384(8)	0.64418(9)	0.64381(8)
	U_{11}	70(2)	51(2)	84(2)	60(2)
	U_{22}	83(2)	62(2)	88(2)	64(2)
	U_{33}	75(2)	59(2)	87(2)	64(2)
	U_{13}	34(2)	26(2)	44(2)	32(2)
	U_{eq}	76(1)	57(1)	85(1)	62(1)
H	*x*	0.104(2)	0.106(2)	0.108(2)	0.109(2)
	y	0.700(2)	0.699(2)	0.716(2)	0.712(2)
	z	0.291(2)	0.290(2)	0.294(2)	0.292(2)
	U_{iso}	222(33)	128(31)	283(37)	208(34)

Table 6. Survey of crystal chemical data at room temperature for selected representatives of the $Mg_{1-x}Fe_x(SO_4)\cdot H_2O$ solid solution series: bond lengths (Å) and angles (°), polyhedral volumes (Å^3), bond strengths (without H atoms; calculated according to Brese and O'Keeffe 1991), and polyhedral distortion parameters (Brown and Shannon 1973; Robinson et al. 1971; Griffen and Ribbe 1979). Data for the kieserite endmember are taken from Bechtold and Wildner (2016).

$Mg_{1-x}Fe_x(SO_4)\cdot H_2O$	$Mg_{1.00}Fe_{0.00}$	$Mg_{0.86}Fe_{0.14}$	$Mg_{0.55}Fe_{0.45}$	$Mg_{0.25}Fe_{0.75}$	$Mg_{0.00}Fe_{1.00}$
x_{Fe}	0.0	0.138(2)	0.450(2)	0.752(3)	1.0
Me–O1 (2×)	2.0216(7)	2.0327(7)	2.0585(7)	2.0854(8)	2.1079(6)
Me–O2 (2×)	2.0414(7)	2.0436(6)	2.0493(6)	2.0545(8)	2.0567(6)
Me–O3 (2×)	2.1714(6)	2.1800(5)	2.1996(5)	2.2183(7)	2.2314(4)
<Me–O>	2.0782	2.0854	2.1025	2.1194	2.1320
$\Delta_{oct}\times10^3$	1.023	1.033	1.070	1.124	1.183
Σ v.u. (Me)	2.15	2.14	2.12	2.10	2.09
O1–Me–O2 (2×) [a]	85.91(3)	85.82(3)	85.59(3)	85.36(3)	85.08(3)
O1–Me–O3 (2×) [a]	88.50(2)	88.19(2)	87.59(2)	86.96(2)	86.48(2)
O2–Me–O3 (2×) [a]	87.20(3)	87.28(3)	87.49(3)	87.67(4)	87.84(3)
σ_{oct}^2	9.75	10.24	11.48	13.16	15.00
V_{oct}	11.901(10)	12.024(8)	12.314(8)	12.604(11)	12.820(8)
S–O1 (2×)	1.4639(7)	1.4629(6)	1.4636(6)	1.4638(8)	1.4638(6)
S–O2 (2×)	1.4817(7)	1.4818(6)	1.4833(6)	1.4849(8)	1.4868(5)
<S–O>	1.4728	1.4724	1.4735	1.4743	1.4753
$BLDP\times10^3$	6.98	7.41	7.72	8.28	9.00
Σ v.u. (S)	6.02	6.03	6.01	6.00	5.98
O1–S–O1'	109.94(6)	109.98(6)	110.11(6)	110.20(8)	110.31(6)
O1–S–O2 (2×)	108.59(4)	108.59(4)	108.73(4)	108.85(4)	108.79(3)
O1–S–O2'(2×)	110.41(4)	110.42(4)	110.24(4)	110.11(5)	110.15(4)
O2–S–O2'	108.89(6)	108.84(5)	108.76(5)	108.70(7)	108.62(5)
σ_{tetr}^2	0.77	0.80	0.64	0.54	0.66
V_{tetr}	1.639(2)	1.638(2)	1.641(2)	1.644(3)	1.648(2)
Me–O1–S	140.38(4)	139.93(4)	138.77(4)	137.58(5)	136.70(4)
Me–O2–S	134.31(4)	134.28(4)	134.06(4)	133.78(5)	133.41(3)
Me–O3–Me	123.27(5)	123.01(4)	122.40(4)	121.80(5)	121.31(4)
Σ v.u. (O1)	1.95	1.95	1.93	1.92	1.91
Σ v.u. (O2)	1.86	1.86	1.86	1.87	1.87
Σ v.u. (O3)	0.55	0.54	0.53	0.53	0.52
O3···O2	2.7449(8)	2.7478(8)	2.7507(8)	2.7541(9)	2.7565(7)
O3–H	0.81(2)	0.76(2)	0.76(2)	0.82(2)	0.82(2)
O2···H	2.01(2)	2.04(2)	2.06(2)	2.01(2)	2.04(2)
O3–H···O2	151(2)	155(2)	150(2)	151(2)	145(2)

[a] plus corresponding obtuse angles.

Table 7. Survey of selected temperature-dependent crystal chemical data for kieserite and szomolnokite, $Mg/Fe(SO_4)\cdot H_2O$: bond lengths (Å) and angles (°), polyhedral volumes ($Å^3$), bond strengths (without H atoms; calculated according to Brese and O'Keeffe 1991), and polyhedral distortion parameters (Brown and Shannon 1973; Robinson et al. 1971; Griffen and Ribbe 1979). Respective room-temperature data for kieserite (Bechtold and Wildner 2016) and szomolnokite are given in Table 6.

$Mg/Fe(SO_4)\cdot H_2O$	$Mg_{1.00}$	$Mg_{1.00}$	$Fe_{1.00}$	$Fe_{1.00}$
T (°C)	–80	–160	–80	–160
Me–O1 (2×)	2.0222(5)	2.0222(5)	2.1093(6)	2.1088(5)
Me–O2 (2×)	2.0407(5)	2.0410(5)	2.0551(5)	2.0546(5)
Me–O3 (2×)	2.1640(4)	2.1607(4)	2.2252(4)	2.2217(4)
<Me–O>	2.0756	2.0746	2.1299	2.1284
$\Delta_{oct}\times10^3$	0.919	0.874	1.110	1.070
Σ v.u. (Me)	2.16	2.17	2.10	2.10
O1–Me–O2 (2×) [a]	85.97(2)	86.03(2)	85.05(2)	85.04(2)
O1–Me–O3 (2×) [a]	88.51(2)	88.56(1)	86.49(2)	86.54(2)
O2–Me–O3 (2×) [a]	87.23(2)	87.27(2)	87.95(2)	88.01(2)
σ_{oct}^2	9.50	9.20	14.92	14.74
V_{oct}	11.861(6)	11.845(6)	12.783(7)	12.758(6)
S–O1 (2×)	1.4640(5)	1.4647(5)	1.4652(5)	1.4657(5)
S–O2 (2×)	1.4837(5)	1.4849(4)	1.4887(5)	1.4901(5)
<S–O>	1.4739	1.4748	1.4770	1.4779
$BLDP\times10^3$	7.72	7.91	9.19	9.53
Σ v.u. (S)	6.00	5.99	5.96	5.94
O1–S–O1'	110.01(4)	110.12(4)	110.47(4)	110.59(4)
O1–S–O2 (2×)	108.61(3)	108.63(2)	108.86(3)	108.85(3)
O1–S–O2'(2×)	110.33(3)	110.30(3)	110.06(3)	110.05(3)
O2–S–O2'	108.94(4)	108.85(4)	108.52(4)	108.42(4)
σ_{tetr}^2	0.71	0.72	0.69	0.76
V_{tetr}	1.643(1)	1.646(1)	1.653(1)	1.656(1)
Me–O1–S	140.00(3)	139.84(3)	136.22(3)	136.04(3)
Me–O2–S	133.63(3)	133.32(3)	132.79(3)	132.45(3)
Me–O3–Me	123.28(3)	123.28(3)	121.28(3)	121.27(3)
Σ v.u. (O1)	1.95	1.95	1.96	1.95
Σ v.u. (O2)	1.86	1.85	1.80	1.80
Σ v.u. (O3)	0.56	0.57	0.53	0.54
O3···O2	2.7292(6)	2.7216(5)	2.7409(6)	2.7316(6)
O3–H	0.81(1)	0.82(1)	0.87(2)	0.85(2)
O2···H	1.98(1)	1.96(1)	1.97(2)	1.95(2)
O3–H···O2	154(1)	156(1)	149(2)	152(1)

[a] plus corresponding obtuse angles.

Table 8. Wavenumber positions of relevant absorption features in FTIR spectra in each measuring mode for the kieserite and szomolnokite endmembers, $Mg/Fe(SO_4)\cdot H_2O$ at room temperature. Linear regression coefficients of the correlations between wavenumber and Fe content (x_{Fe}) are listed. Positions of weak yet important bands observed in the region of H_2O combination modes are given in the scope of DRIFT measurements on undiluted sample material.

Transmission (1:300 sample dilution in KBr)				
Vibration	**Wavenumber position (cm^{-1})**		**Linear regression coefficients** [a]	
	Kieserite	Szomolnokite	**a**	**b**
Peak 850 cm^{-1}	884(1)	831(2)	-57.5(1)	887.8(8)
$\nu_{1(SO_4)}$	1043(1)	1015(1)	-29.6(1)	1040(1)
$\nu_{3(SO_4)main}$	1165(1)	1133(1)	-27.8(1)	1162.1(8)
$\nu_{2(H_2O)}$	1525(4)	1496(2)	-32.1(1)	1528.9(8)
$\nu_{1(H_2O)}$	3182(4)	3245(4)	67.2(3)	3188(2)
$\nu_{3(H_2O)}$	3367(12)	3391(10)	1.3(1)	3388(5)
Attenuated Total Reflectance (ATR)				
Vibration	**Wavenumber position (cm^{-1})**		**Linear regression coefficients** [a]	
	Kieserite	Szomolnokite	**a**	**b**
Peak 850 cm^{-1}	866(3)	810(1)	-54.7(2)	861(1)
$\nu_{2(H_2O)}$	1520(1)	1491(2)	-30.57(7)	1522.2(4)
$\nu_{1(H_2O)}$	3165(4)	3217(5)	57.5(3)	3157(2)
$\nu_{3(H_2O)}$	3345(8)	3340(10)	0.8(7)	3342(4)
Diffuse Reflectance (1:20 sample dilution in KBr)				
Vibration	**Wavenumber position (cm^{-1})**		**Linear regression coefficients** [a]	
	Kieserite	Szomolnokite	**a**	**b**
Peak 850 cm^{-1}	886(3)	839(1)	-57.2(2)	895.4(1)
$\nu_{1(SO_4)}$	1044(2)	1018(1)	-27.6(1)	1042(1)
$\nu_{3(SO_4)\ center}$	1172(3)	1139(2)	-21.3(2)	1158(2)
$\nu_{2(H_2O)}$	1523(1)	1494(1)	-29.38(6)	1523(4)
$\nu_{1(H_2O)}$	3180(2)	3249(5)	70.8(2)	3180(1)
$\nu_{3(H_2O)}$	3365(13)	3383(21)	1.7(6)	3359(3)
Diffuse Reflectance (undiluted samples)				
Vibration	**Wavenumber position (cm^{-1})**		**Linear regression coefficients** [a]	
	Kieserite	Szomolnokite	**a**	**b**
Peak 600 cm^{-1}	690(1)	678(1)	-11.6(1)	688.5(7)
Reststrahlenband	1316(6)	1283(5)	-30.1(2)	1312(1)
$\nu_{2(H_2O)}$	1526(3)	1496(2)	-30.7(3)	1528(2)
$\nu_{1(H_2O)}$	3203(20)	3304(9)	88.8(1)	3209(5)
$\nu_{3(H_2O)}$	3412(23)	3431(9)	2.3(1)	3405(6)
Peak 4700 cm^{-1}	4688(4)	4749(5)	---	---
Peak 4850 cm^{-1}	4845(3)	4854(6)	---	---
Peak 5090 cm^{-1}	5087(10)	5021(11)	---	---

[a] Linear regression equation $y = \mathbf{a}(x_{Fe}) + \mathbf{b}$, where y denotes the wavenumber position of the vibration mode.

Table 9. Wavenumber shift positions of relevant bands in Raman spectra for the kieserite and szomolnokite endmembers, $Mg/Fe(SO_4)\cdot H_2O$. Linear regression coefficients of the correlations between band position and the Fe content (x_{Fe}) are listed. Additionally, changes in the band position with decreasing temperature are given for all relevant Raman bands.

Peak assignment	Raman shift position at RT (cm^{-1})		Linear regression coefficients [a]		Band shift with temperature decrease ($\times10^{-2}$ cm^{-1} / °C)
	Kieserite	Szomolnokite	**a**	**b**	
Lattice modes	125.3(1)	112.4(4)	-10.7(6)	123.7(3)	4.66
$\nu_{transl\ Fe\text{-}H_2O}$	219.2(1)	218.0(1)	-0.4(5)	219.2(3)	3.43
$\nu_{2(SO_4)\_1}$	432.2(1)	422.8(1)	-9.4(3)	432.2(2)	-1.95
$\nu_{2(SO_4)\_2}$	502.1(1)	493.8(1)	-7.2(3)	501.2(2)	-1.61
$\nu_{4(SO_4)\_1}$	628.7(4)	616.6(2)	-11.78(4)	628.1(2)	0.85
$\nu_{4(SO_4)\_2}$	633.8(2)	623(1)	-10.1(5)	633.0(3)	-0.55
$\nu_{1(SO_4)}$	1041.8(1)	1017.6(1)	-24.9(1)	1040.9(6)	-0.47
$\nu_{3(SO_4)\_1}$	1101.6(1)	1071.0(5)	-28.7(1)	1101.2(8)	-1.82
$\nu_{3(SO_4)\_2}$	1118.9(1)	1090.4(7)	-29.1(1)	1121(1)	-0.51
$\nu_{3(SO_4)\_3}$	1216.7(1)	1195.0(1)	-22.0(9)	1215(5)	2.22
$\nu_{2(H_2O)}$	1508.3(1)	1477.6(1)	-27.1(3)	1501(2)	2.22
$\nu_{1(H_2O)}$	3178(2)	3247(5)	53.0(6)	3189(4)	-16.57
$\nu_{3(H_2O)}$	3388(4)	3368(12)	-9(1)	3372(6)	15.25

[a] Linear regression equation $y = \mathbf{a}(x_{Fe}) + \mathbf{b}$. where y denotes the Raman shift position.

This is a preprint, the final version is subject to change, of the American Mineralogist (MSA)
Cite as Authors (Year) Title. American Mineralogist, in press.
DOI: https://doi.org/10.2138/am-2019-6983

1174 **Table 10.** Summary of results from classical crystal field (CF) and superposition model (SM)
1175 calculations for Fe^{2+} in szomolnokite, based on observed transitions energies as indicated in Fig.
1176 15. Fixed SM parameters are R_0=2.13 Å, t_4=5, t_2=3. All given values are in cm^{-1} except the ratio
1177 C/B (fixed at 4.3) and the nephelauxetic ratio β. Racah B_0 and C/B are taken from Figgis and
1178 Hitchman (2000).
1179

Szomolnokite	SM (triclinic)	'classical' CF (tetragonal)
Dq_{cub}	–	855
Dq_{eq}	–	878
Dt	–	40
Ds	–	660
Racah B (C/B=4.3)	835	840
β (B_0=897 cm^{-1})	0.93	0.94
Dq_{cub} (from s_4)	826	855
$\overline{B}_4$	4920	–
$\overline{B}_2$	8900	–
s_4	7573	7838
s_2	2319	2066

1180
1181

1182 **Figures**

1183

1184

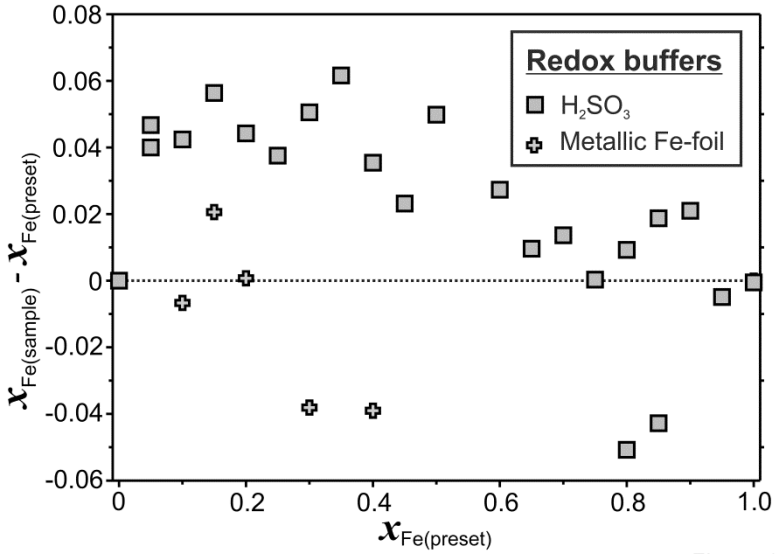

1185 Figure 1

1186

1187

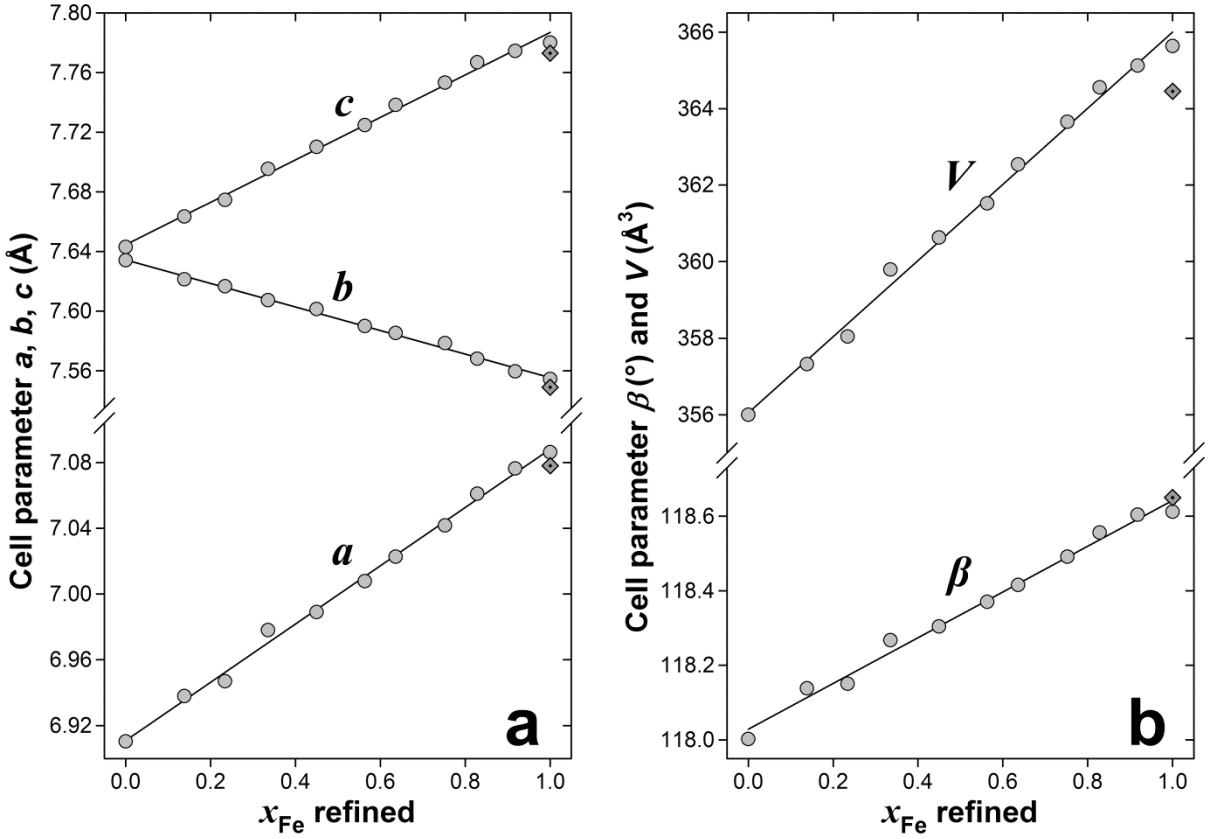

1188 Figure 2

1189

This is a preprint, the final version is subject to change, of the American Mineralogist (MSA)
Cite as Authors (Year) Title. American Mineralogist, in press.
DOI: https://doi.org/10.2138/am-2019-6983

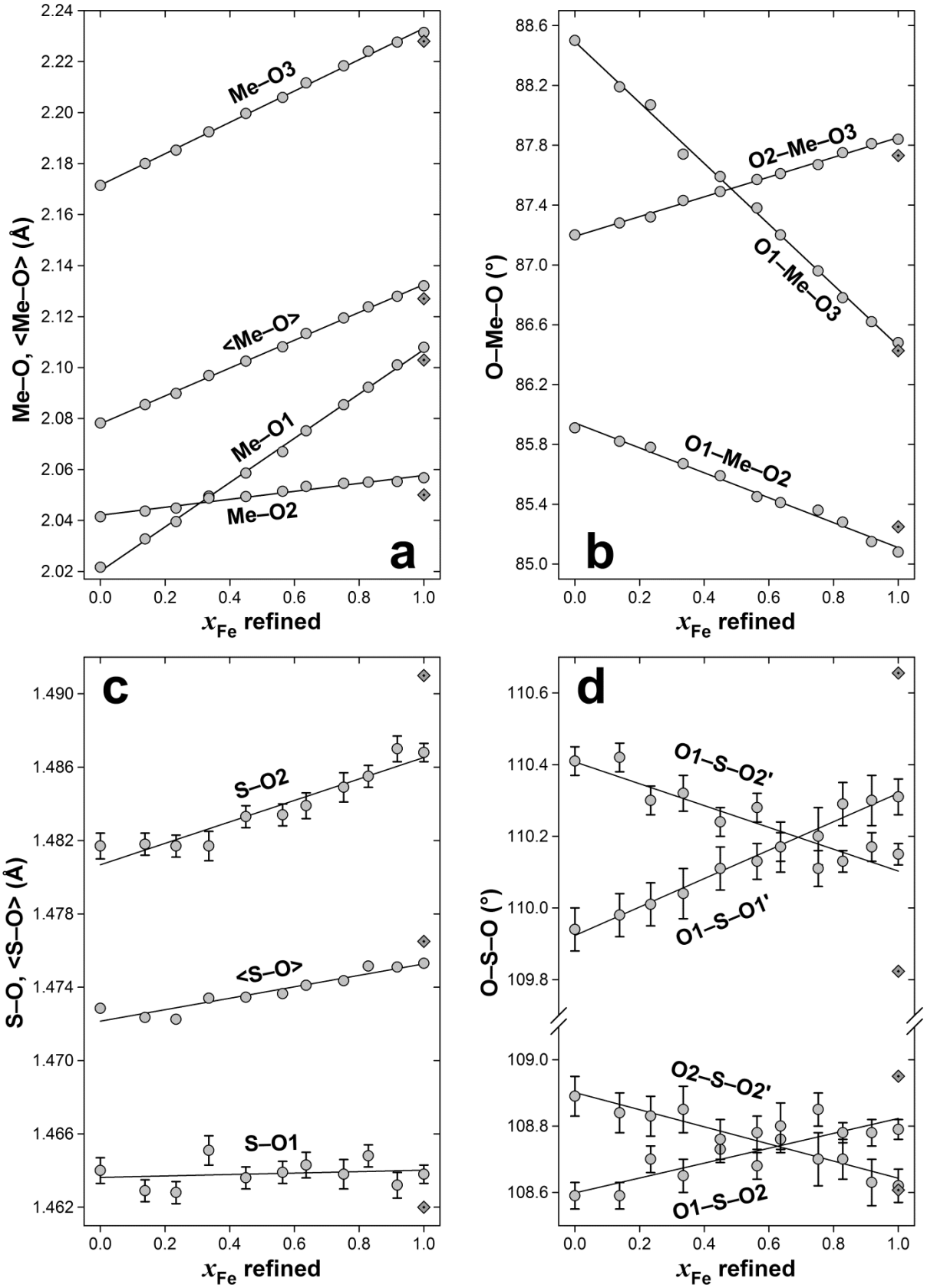

Figure 3

This is a preprint, the final version is subject to change, of the American Mineralogist (MSA)
Cite as Authors (Year) Title. American Mineralogist, in press.
DOI: https://doi.org/10.2138/am-2019-6983

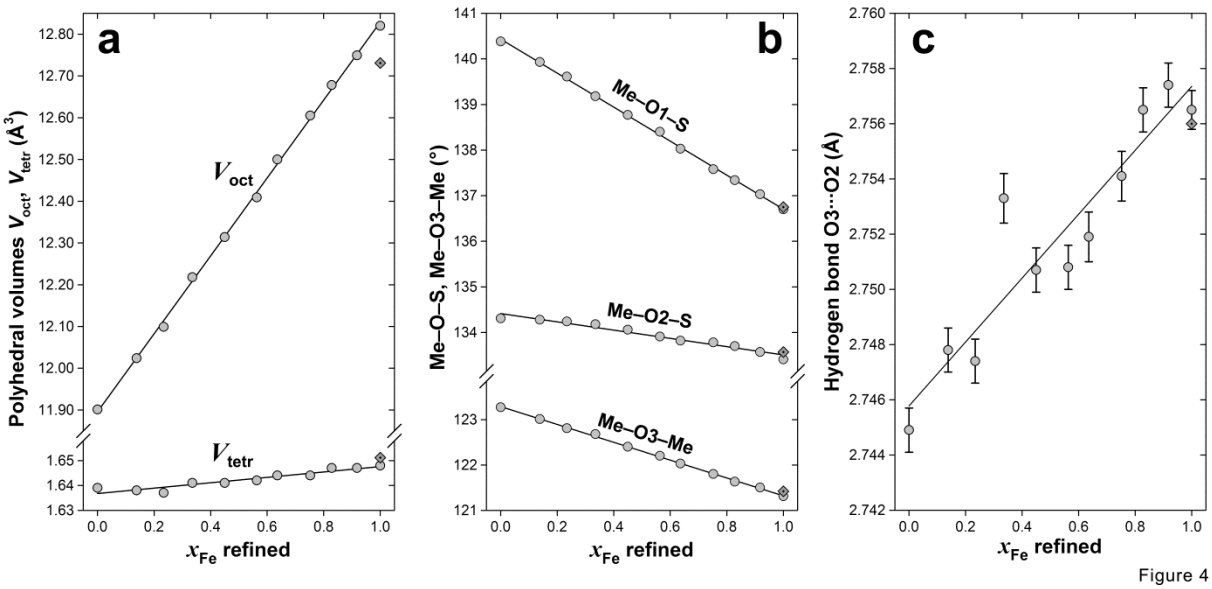

Figure 4

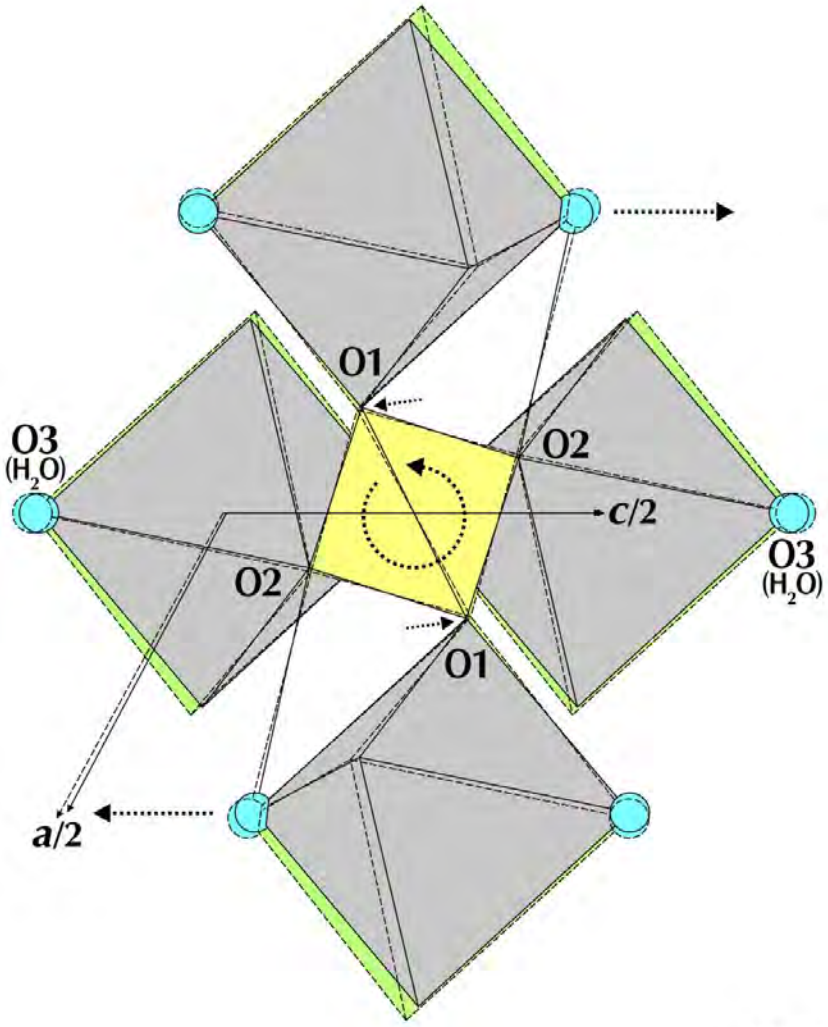

Figure 5

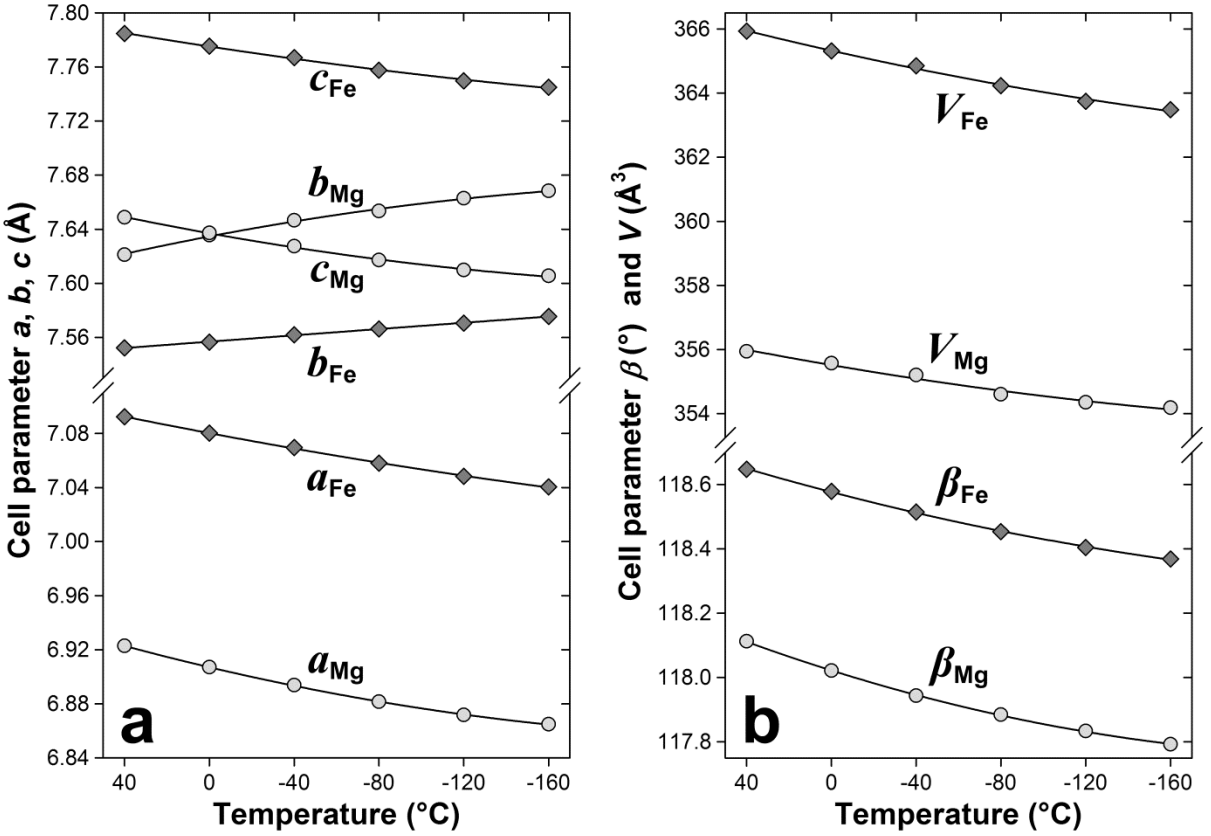

Figure 6

This is a preprint, the final version is subject to change, of the American Mineralogist (MSA)
Cite as Authors (Year) Title. American Mineralogist, in press.
DOI: https://doi.org/10.2138/am-2019-6983

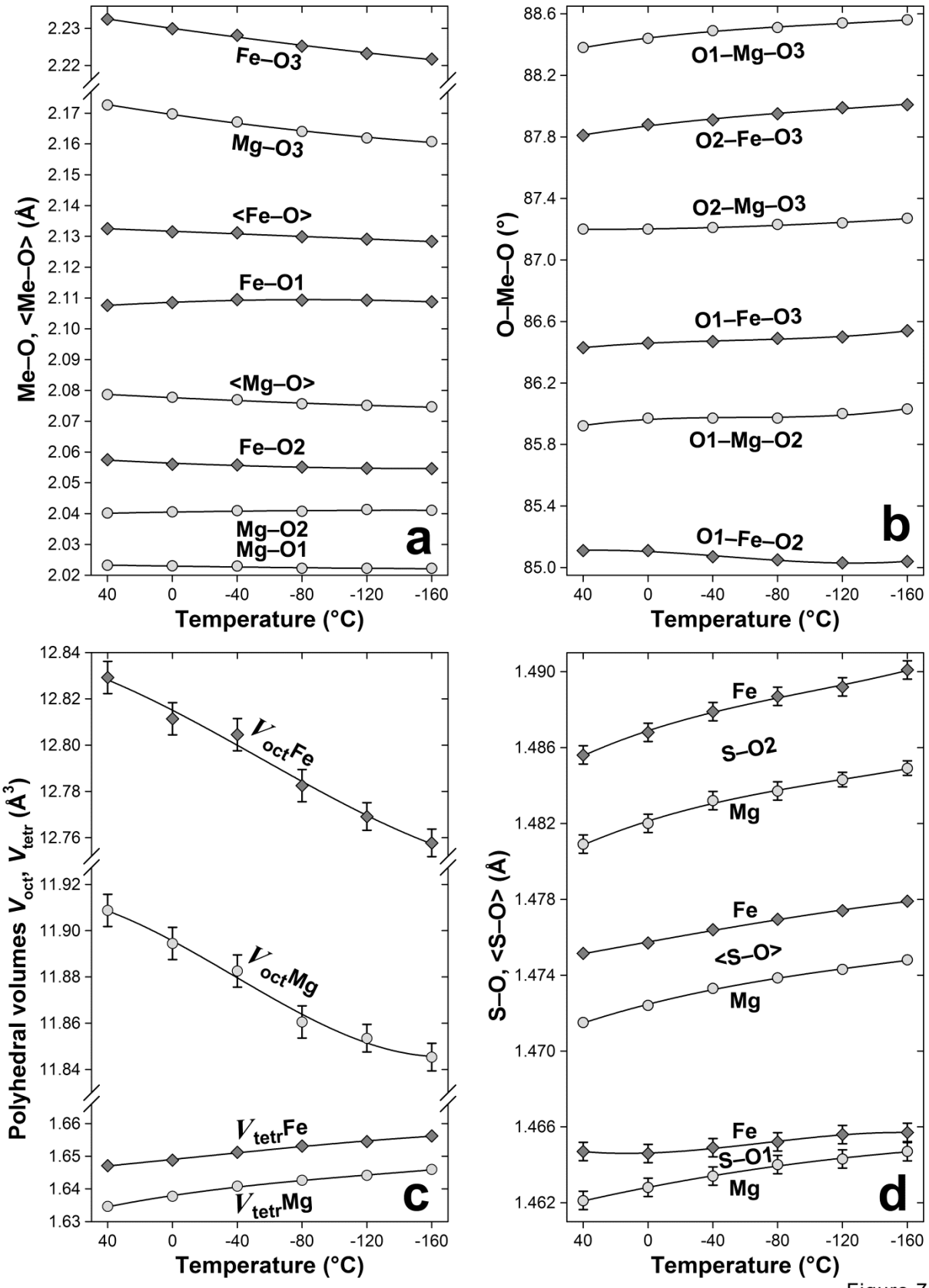

Figure 7

1202

1203

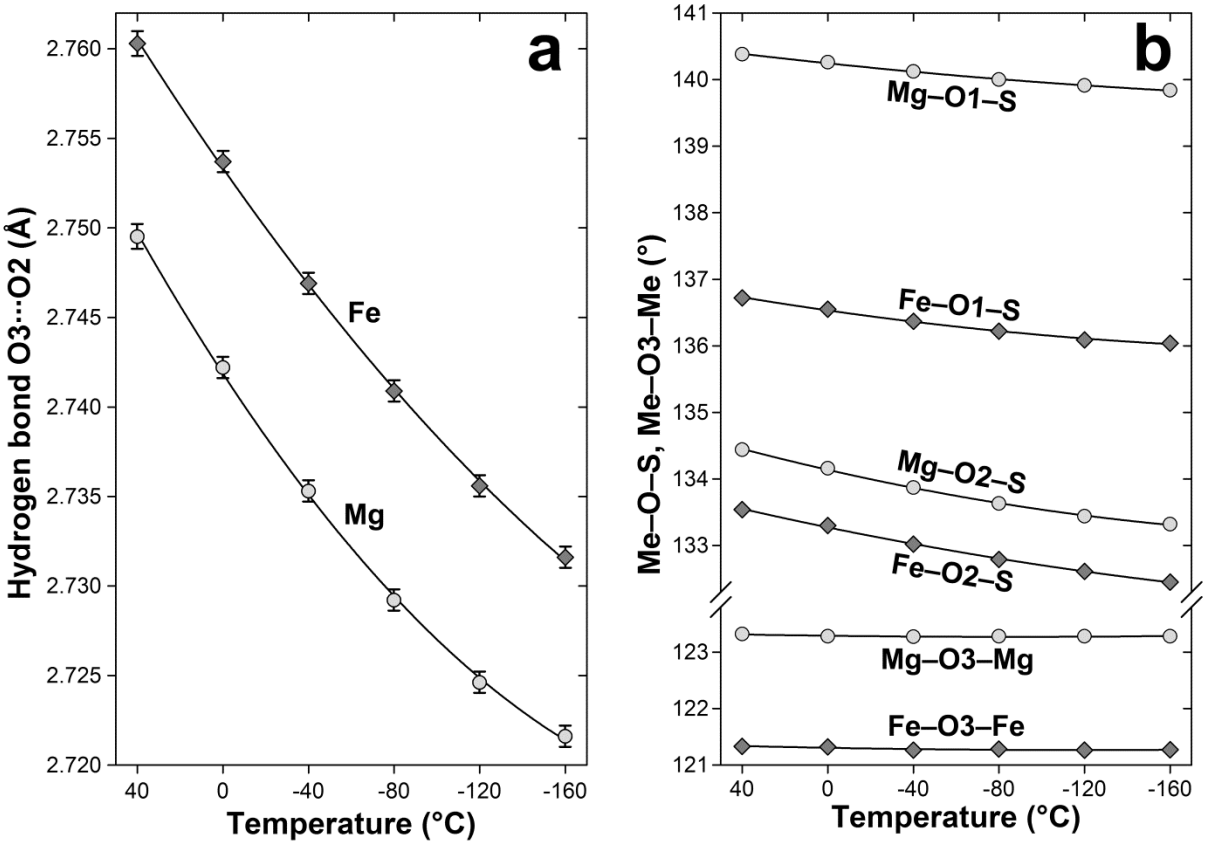

1204 Figure 8

1205

1206

1207

1208

This is a preprint, the final version is subject to change, of the American Mineralogist (MSA)
Cite as Authors (Year) Title. American Mineralogist, in press.
DOI: https://doi.org/10.2138/am-2019-6983

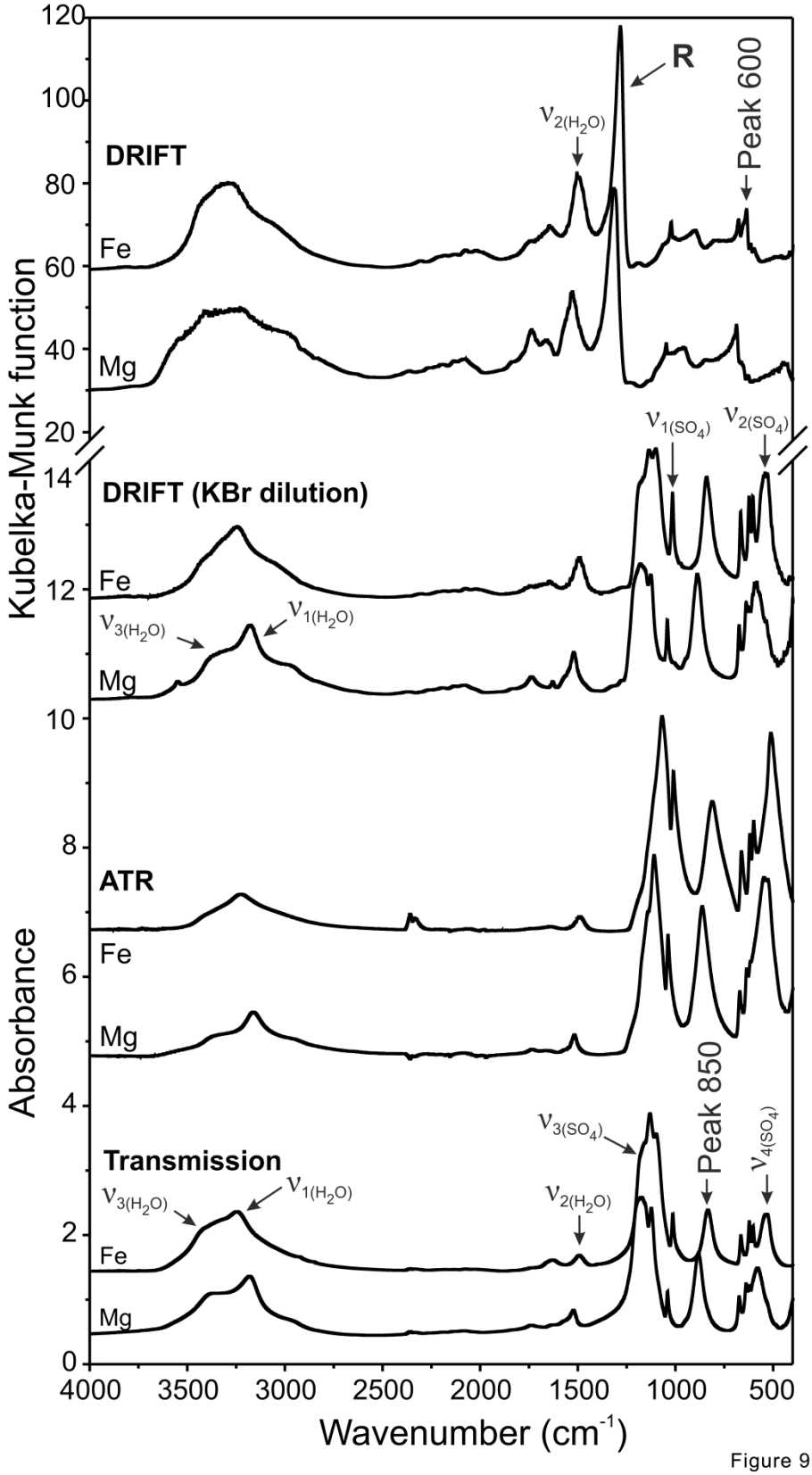

1209 Figure 9

This is a preprint, the final version is subject to change, of the American Mineralogist (MSA)
Cite as Authors (Year) Title. American Mineralogist, in press.
DOI: https://doi.org/10.2138/am-2019-6983

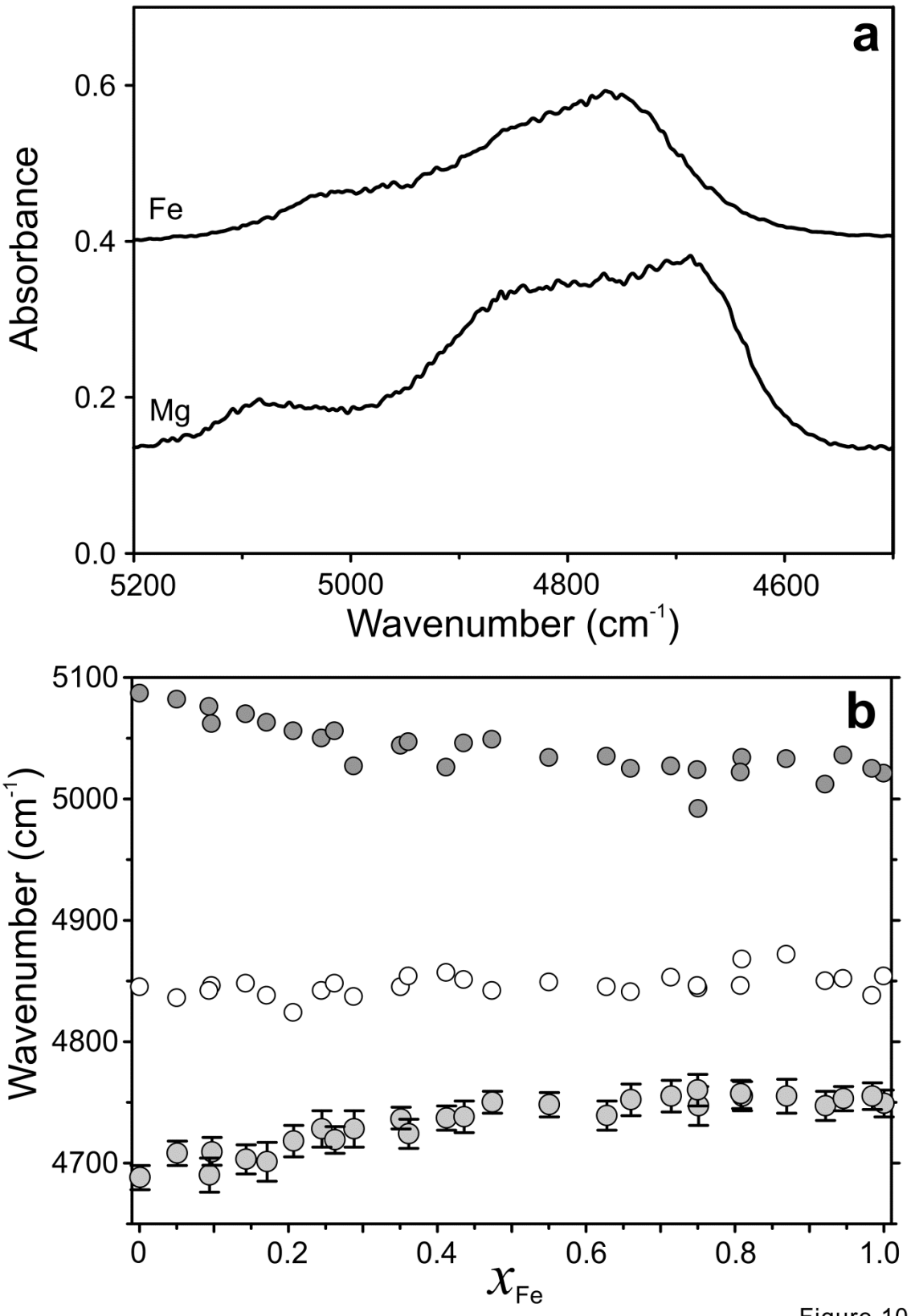

Figure 10

This is a preprint, the final version is subject to change, of the American Mineralogist (MSA)
Cite as Authors (Year) Title. American Mineralogist, in press.
DOI: https://doi.org/10.2138/am-2019-6983

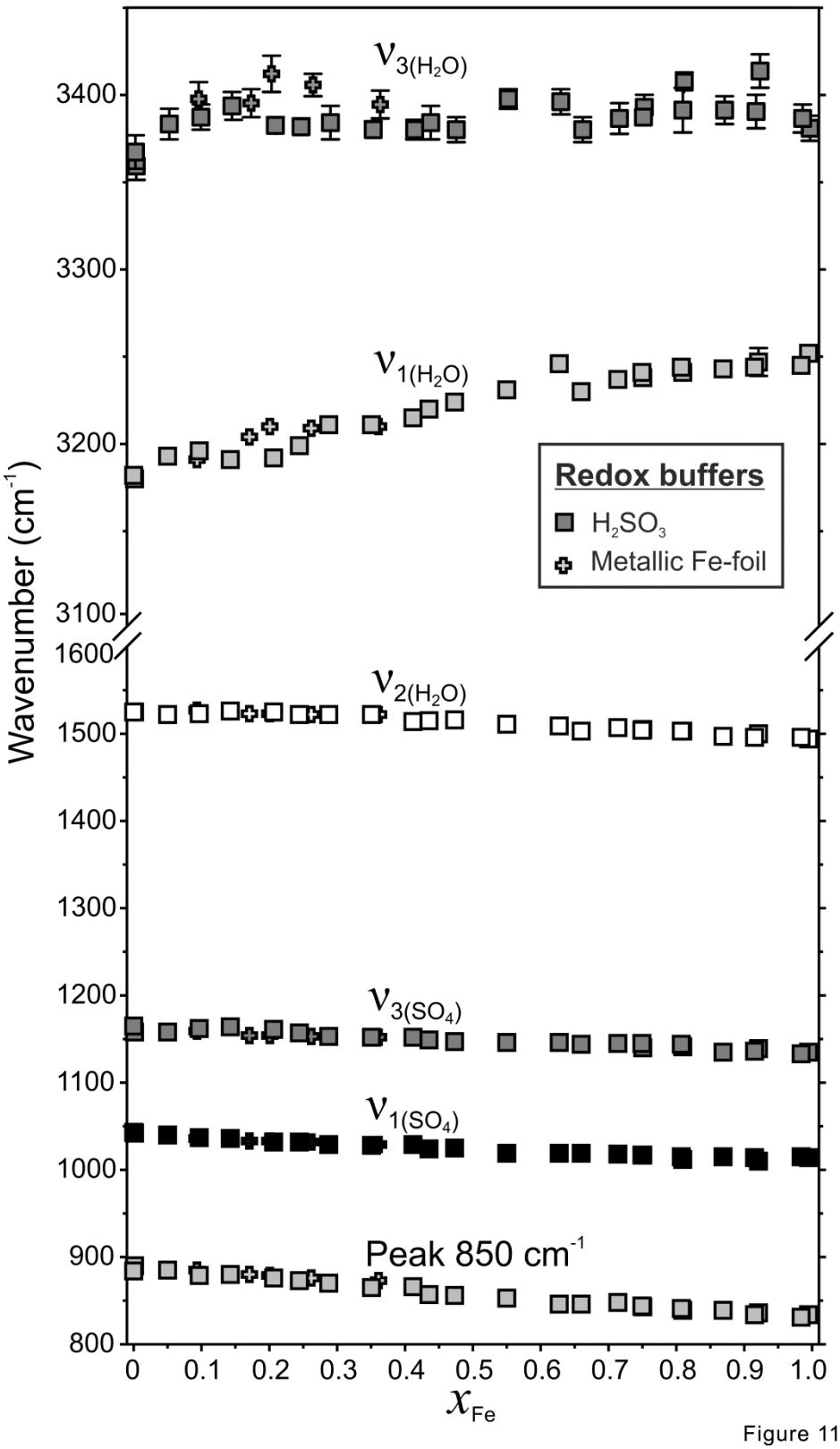

Figure 11

This is a preprint, the final version is subject to change, of the American Mineralogist (MSA)
Cite as Authors (Year) Title. American Mineralogist, in press.
DOI: https://doi.org/10.2138/am-2019-6983

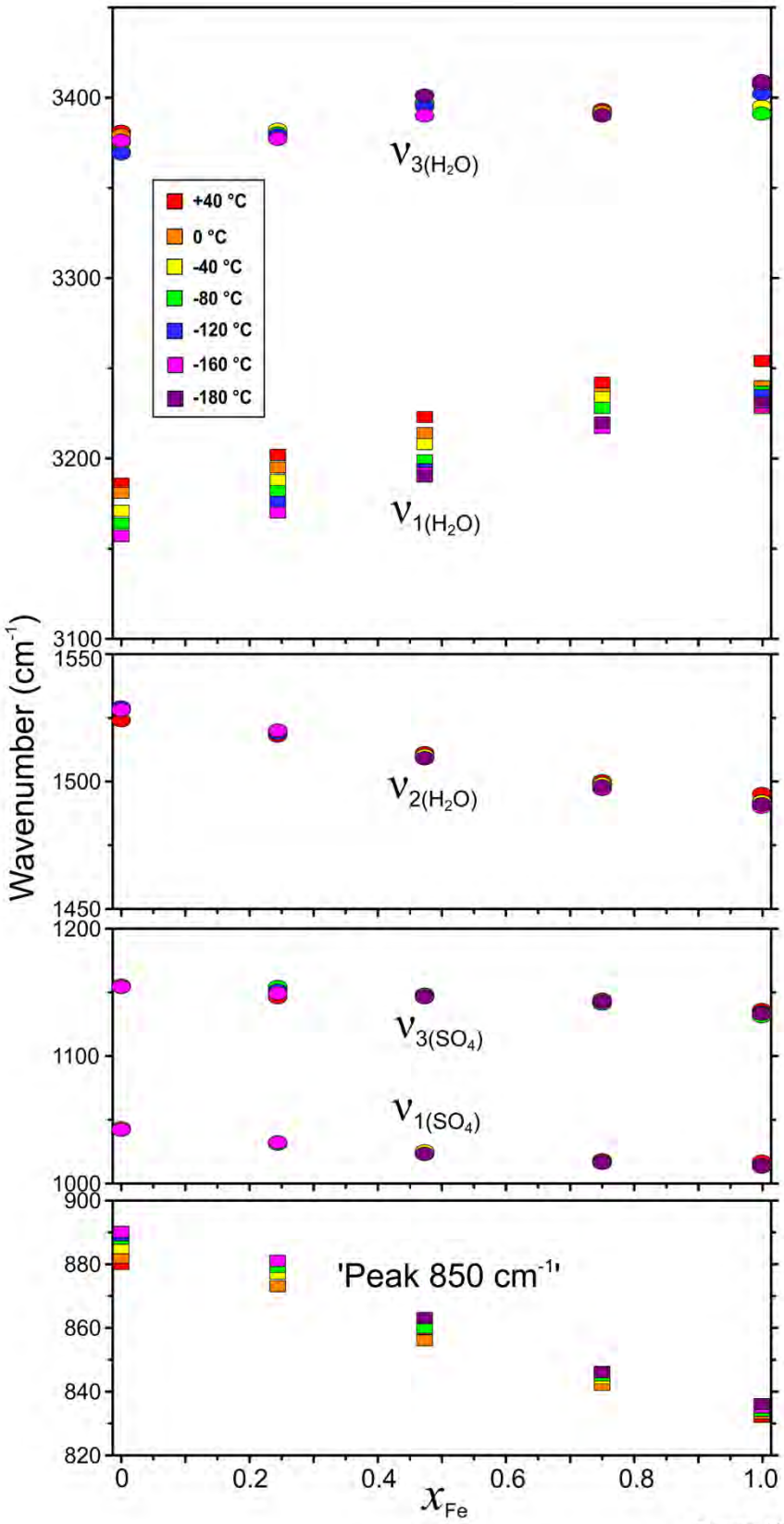

Figure 12

This is a preprint, the final version is subject to change, of the American Mineralogist (MSA)
Cite as Authors (Year) Title. American Mineralogist, in press.
DOI: https://doi.org/10.2138/am-2019-6983

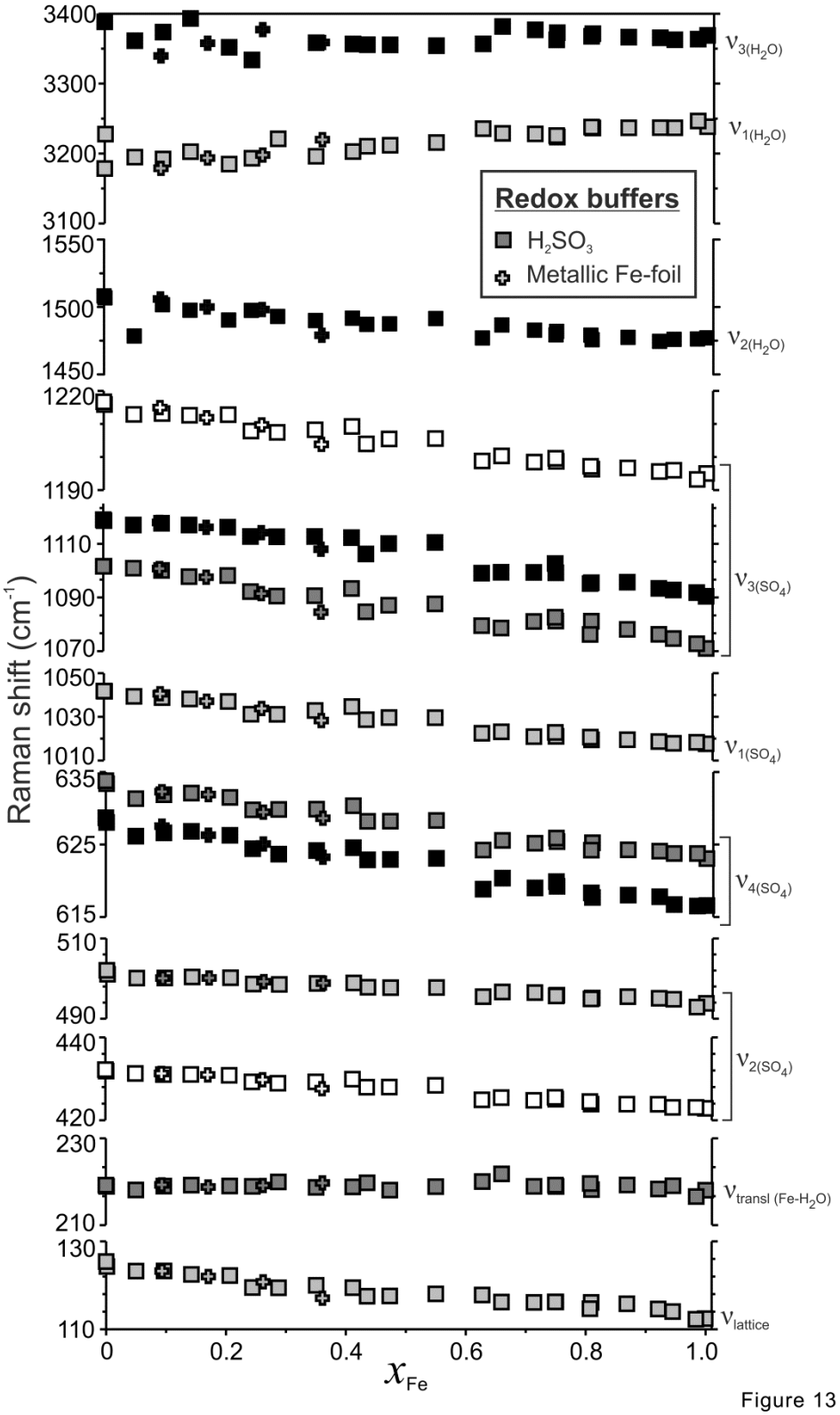

Figure 13

This is a preprint, the final version is subject to change, of the American Mineralogist (MSA)
Cite as Authors (Year) Title. American Mineralogist, in press.
DOI: https://doi.org/10.2138/am-2019-6983

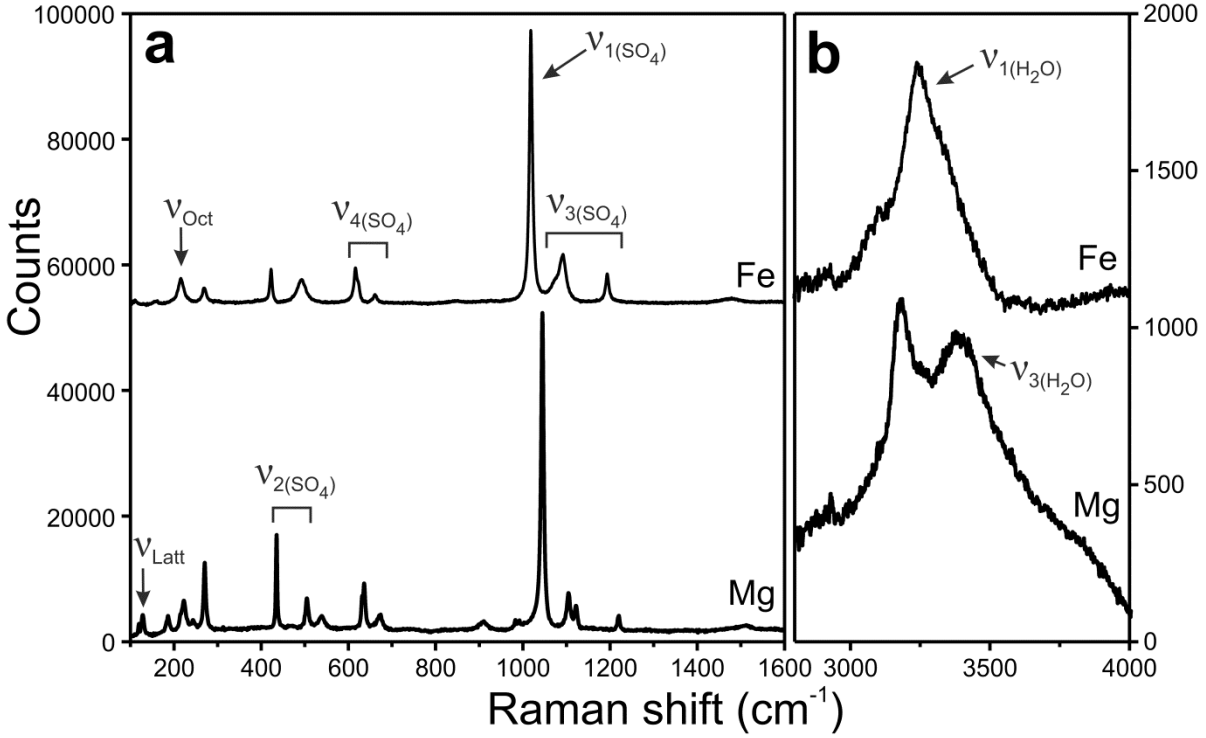

Figure 14

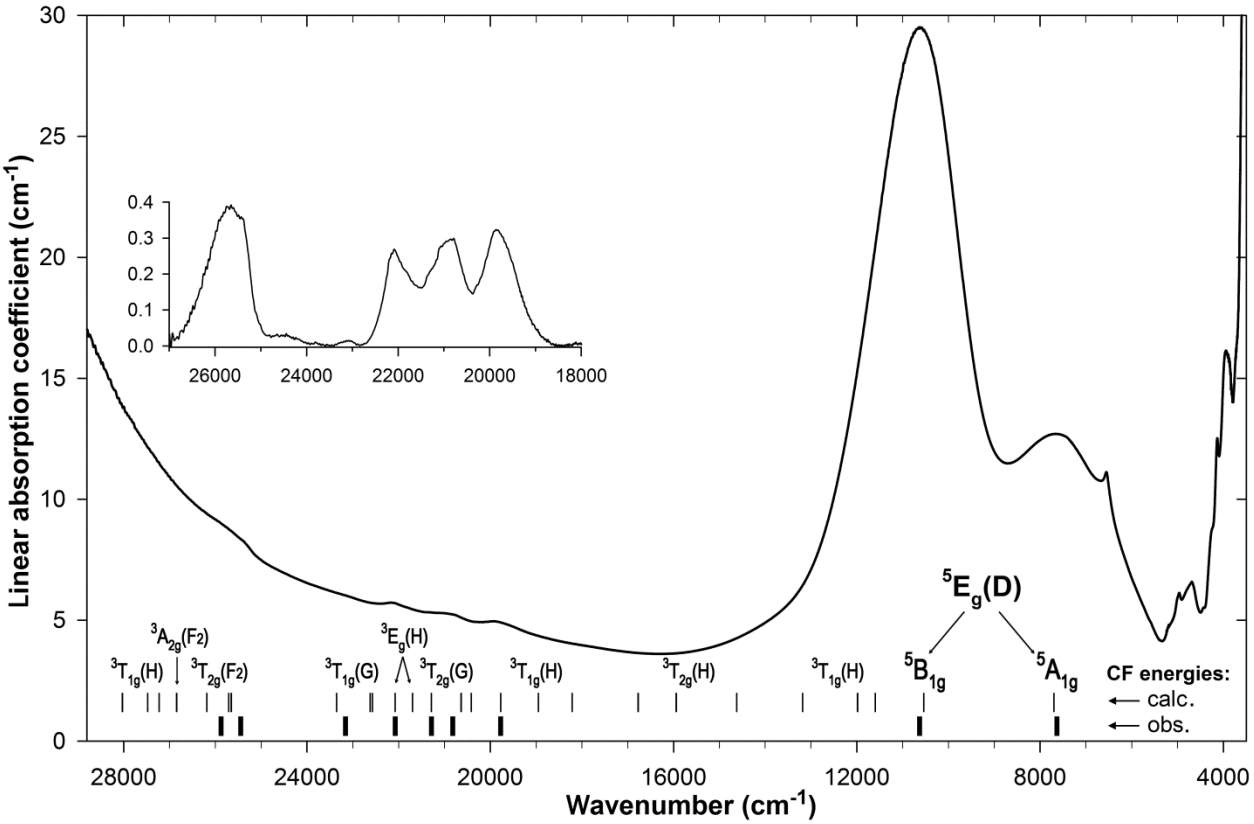

Figure 15